A Comparative Study on Fatigue Indicator Parameters for Near-α Titanium Alloys

Yang Liu[1*], Xiang Zhang[2] and Caglar Oskay[3]

1 Department of Materials, Imperial College London, London SW7 2AZ, United Kingdom

2 Department of Mechanical Engineering, University of Wyoming, Laramie, WY 82071, USA

3 Department of Civil and Environmental Engineering, Vanderbilt University, Nashville, TN 37235, USA

* Corresponding author, Tel.: 44-7523904774, Email: yang.liu@imperial.ac.uk

Abstract

Nucleation of in-service cracks leads to detrimental consequences for structural components of near-α titanium alloys subjected to fatigue loads. Experimental observations show that the fatigue initiation facets usually form in certain crystallographic orientation ranges of 'hard' primary α grains which differ between pure and dwell fatigue loads. In this manuscript, a comparative study has been performed using several fatigue indicator parameters (FIPs) to assess their ability to predict the location of fatigue crack nucleation in near -α titanium alloy microstructures. All selected FIPs are implemented within the same polycrystalline plasticity finite element modelling framework to facilitate one-to-one comparisons. Comparison on predictability of critical initiation locations and their crystallographic orientations is studied for incorporated FIPs under pure and dwell fatigue. The critical locations predicted by some FIPs were found to be close to each other, and consistent with the crystallographic orientation ranges from fractography measurements, in addition to the range transition from pure to dwell fatigue loads. Critical locations from slip driven FIPs are obtained to be several grains away from that of the former ones and are inclined to capture orientations of slip traces from experiments.

1. Introduction

Near-α titanium alloys are widely used in turbofan engines and airframes due to their light weight, high fatigue strength, fracture toughness and excellent corrosion resistance. Near-α titanium alloys are subjected to fatigue and dwell fatigue loads at relatively low temperature (*T*

< $0.4T_m$), in the service conditions of engine and airframe components such as compressor discs and air-panels. Under these loading conditions, fatigue crack nucleation tends to occur in the grain boundaries between neighbouring hard and soft grains [1–4]. Fatigue crack nucleation could take up nearly 90% of the total fatigue life [5–8].

Characteristic crack facets are observed in the near-α titanium alloys under fatigue or dwell fatigue loading conditions, which are mostly cleavage facet surfaces surrounded by grains with rough facets. The 'penny'-shaped crack initiation results from the trans-granular fracture across the primary-α grains whereas the rough surface forms due to the slip activation and the corresponding sessile dislocations pinning inside the shear bands [9]. Fig 1 (a) shows that fatigue crack nucleation tends to occur in the hard micro-texture regions (MTR) or grains where their c-axes point towards the loading direction. Dashed region is initial facet formation region, which contains hard grains with angles < 30° between their c-axes and loading direction. These angles are referred as the 'mismatch angles' in the following context. Surrounding regions contains soft grains, with their mismatch angles mostly > 45° [8]. A specific example in Fig 1 (b) [10] shows the penny-shaped facet nucleation inside a hard grain, indicated as '1' and a relatively soft neighbouring grain '2' is observed with rough surface, indicating shear bands and dislocation pile-ups. The crack is observed to initiate right between the hard-soft grain pair, which demonstrates the theory proposed by Stroh [4], where dislocation pile-ups in the soft grain raise stresses at the grain boundary of hard-soft grain pair, leading to crack nucleation in the hard grain. The crystallographic orientations of the initiated facets fall into certain range of mismatch angles during different loading conditions. Under pure fatigue load, the mismatch angle of the facets lies in the range of 0^o to 10^o [7,11,12]. In contrast, the mismatch angles under dwell fatigue load are in the range of 10^o to 20^o [7,13] inside relatively 'softer' hard crystals with their c-axes pointing slightly away from loading direction.

For the past 20 years, multiple fatigue indicator parameters (FIPs) and fatigue initiation drivers (FIDs) were proposed for predicting the fatigue initiation site of metallic materials under fatigue load [3,9,13–19]. Physical-based crystal-level FIPs have been proposed as functions of local mechanical and physical quantities [3,9,14–16]. Crack nucleation sites [13–15,17,18], crystallography [13,14,19] and microstructure-sensitive lifetimes [3,13,19,20] are investigated using the FIPs under fatigue or dwell fatigue loading conditions. For modelling fatigue crack nucleation in near-α titanium alloys, there is still open question of how and which independent physical variables or combinations thereof could be best linked to the fatigue crack nucleation sites. In addition, previously proposed FIPs were assessed using different crystal

plasticity finite element (CPFE) modelling frameworks, which makes it hard to compare their predictive capabilities. In this work, a consistent crystal plasticity framework is developed to incorporate a number of FIPs and FIDs for a comparative study.

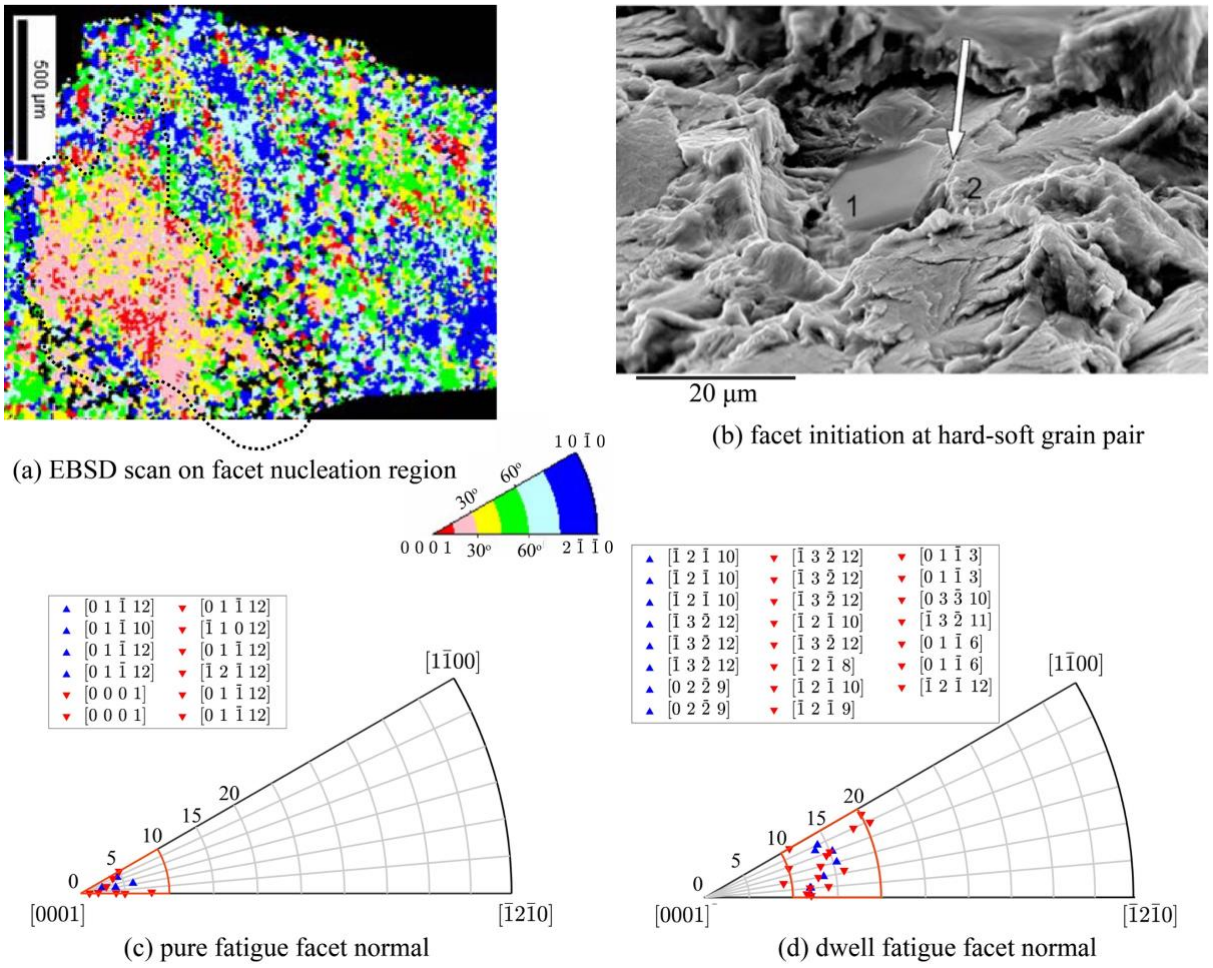

Fig 1 Preferential facet nucleation at hard-soft grain pair in near-α Ti-6242 alloys. (a) facet nucleation at the hard microtextured region (enclosed by dotted line) neighboring to soft grains [8]. *(b) penny-shaped facet nucleation site at the hard grain neighboring to a soft grain with a rough surface* [10]. *(c) and (d) show the facet nucleation sites with preferential mismatch angle ranges [0°, 10°] and [10°, 20°] under pure fatigue* [7,11,12] *and dwell fatigue* [7,13]*, respectively. Experimental data with upward triangles are from* [7,11] *whereas the downward ones are from* [12,13].

Dislocation density has been an important contributor to fatigue indicator parameters in near-α titanium alloys [1,3,20–23]. At a lower length scale, experimental observations using high resolution electron backscatter diffraction (HR-EBSD) [24] and transmission electron microscopy (TEM) [25,26] indicate that the dislocation activation in the soft grain and pile-ups at the hard-soft grain boundaries lead to the stress accumulation in the neighbouring hard grain for near-α titanium alloys. Fatigue resistance is intrinsically linked with dislocation relaxation

or accumulation, through cyclic dislocation reversal [27], slip transfer [25,27,28] and source-activation [25,29]. However, till now, dislocation density alone has not been directly linked to the fatigue crack nucleation in near-α titanium alloys. Enlightened by experimental observations in TEM and associated discrete dislocation work showing a high density mismatch of dislocations at hard-soft grain boundary in near-α titanium alloys [26,27], a new fatigue indicator parameter was recently proposed based on the maximum dislocation density discrepancy among all grain pairs in near-α titanium alloys [30]. In addition to its physical basis, this FIP is well suited for implementation in reduced order and multiscale models to predict fatigue initiation at both microstructure and component scales [30–33], as well as in uncertainty quantification associated with fatigue crack nucleation [34].

In this study, the new FIP solely based on dislocation density is first validated with experimental data and then compared with a number of existing FIPs within one CPFE framework aiming to test their predictive capability of fatigue crack nucleation over statistical volume elements (SVEs). The predictability tested includes not only the location of fatigue crack initiation, but also the crystallographic orientations of the critical fatigue nucleation site. The remainder of this manuscript is organized as follows. A crystal plasticity model incorporating dislocation reversal is introduced and the reconstruction of SVEs is verified based on experimental EBSD and data of near-α Ti-6242 alloy in Section 2. The FIPs are incorporated in the current CPFE framework and validated against the crystallographic characteristics are discussed in Section 3. In Section 4, a comparative study is performed to investigate the accuracy of FIPs with respect to critical site locations and their crystallographic orientations in the context of polycrystalline SVEs, subjected to pure and dwell fatigue loads. Conclusions are drawn in Section 5.

2. Methodology

2.1 Crystal plasticity framework incorporating reversible dislocation evolution

In this study, the finite strain elasto-plastic framework is employed with the total deformation gradient $\mathbf{F}$ multiplicatively decomposed into plastic deformation gradient $\mathbf{F}^p$ and elastic deformation gradient $\mathbf{F}^e$,

$$\mathbf{F} = \mathbf{F}^e\mathbf{F}^p \tag{1}$$

The plastic velocity gradient $\mathbf{L}^p$, is expressed as the sum of directional dislocation slip contributions from all crystallographic slip systems.

$$\mathbf{L}^p = \dot{\mathbf{F}}^p(\mathbf{F}^p)^{-1} = \sum_{\kappa} \dot{\gamma}^{\kappa}\, \mathbf{s}^{\kappa} \otimes \mathbf{n}^{\kappa} \tag{2}$$

where $\dot{\gamma}^{\kappa}$ is the slip rate in κ^{th} slip system, and $\mathbf{s}^{\kappa}$ and $\mathbf{n}^{\kappa}$ are the slip direction and slip normal of this slip system. The dislocations are activated and slip rate becomes non-zero when the magnitude of resolved shear stress τ^{κ} exceeds the critical resolved shear stress (CRSS) τ_c^{κ}. By considering both forward and backward dislocation jumps, the slip rate is derived from the Orowan equation [2],

$$\dot{\gamma}^{\kappa} = \rho_m v (b^{\kappa})^2 \exp\left(-\frac{\Delta F}{k\theta}\right) \sinh\left(\frac{\Delta V}{k\theta}(|\tau^{\kappa}| - \tau_c^{\kappa})\right) \tag{3}$$

where b^{κ} is the Burgers vector magnitude of the slip system, ρ_m the mobile dislocation density, v the average dislocation glide velocity, k the Boltzmann constant and θ the Kelvin temperature. The thermal activation energy ΔF and activation volume ΔV are the predominant factors controlling the strain rate sensitivity of the material. Hyperbolic sine form ensures the accurate strain rate sensitivity description at quasi-static and dynamic strain rates [35].

The hardening mechanism in each slip system links with the dislocation densities, and the slip strength τ_c^{κ} is additively split into three parts, the initial strength $\tau_{c,0}^{\kappa}$, dislocation induced strength contributions $\tau_{\text{for}}^{\kappa}$ and $\tau_{\text{deb}}^{\kappa}$, due to pinning of forest dislocation and dislocation debris, respectively,

$$\tau_c^{\kappa} = \tau_{c,0}^{\kappa} + \tau_{\text{for}}^{\kappa} + \tau_{\text{deb}}^{\kappa} \tag{4}$$

The sessile forest dislocation and geometrically necessary dislocation (GND) are the main source of slip strengthening. The former accumulates from sub-grain slip activation and the latter accommodates the lattice distortion near grain boundaries [27,36,37]. For hexagonal-close-packed (HCP) crystal, the sub-grain slip system and dislocation interaction is relatively low. Experimental observations showed that dominant single slip system activations were observed in primary-α grains and dislocation interactions occur mostly near grain boundaries [26,28,38], which leads to intense dislocation interaction between forest dislocations and GNDs. Thus, the strength increase $\tau_{\text{for}}^{\kappa}$ needs to consider both GND and forest dislocations,

$$\tau_{\text{for}}^{\kappa} = \mu\chi b^{\kappa}\sqrt{\rho_{\text{for}}^{\kappa} + \rho_{\text{GND}}^{\kappa}} \tag{5}$$

where μ is the shear modulus. χ is the interaction coefficient, defined as 0.9 due to low dislocation interactions [39], and $\rho_{\text{for}}^{\kappa}$ and $\rho_{\text{GND}}^{\kappa}$ are the densities of forest dislocations and GNDs, respectively.

GND density is computed based on the plastic deformation gradient [2,36,37],

$$\sum_{\kappa}(\mathbf{b}^{\kappa}\otimes\boldsymbol{\rho}_{\text{GND}}^{\kappa}) = \text{curl}(\mathbf{F}^{p}) \tag{6}$$

where the summation is over all active slip systems including screw and edge type dislocations. According to [2,40,41], a GND vector $\boldsymbol{\rho}_{\text{GND}}^{\kappa} = \left[\rho_{\text{GND},s}^{\kappa}\ \rho_{\text{GND},n}^{\kappa}\ \rho_{\text{GND},m}^{\kappa}\right]^{\text{T}}$ is defined along $\mathbf{s}^{\kappa}$ and $\mathbf{n}^{\kappa}$ and $\mathbf{m}^{\kappa} = \mathbf{s}^{\kappa} \times \mathbf{n}^{\kappa}$ directions, respectively, and $\rho_{\text{GND}}^{\kappa}$ is the L^2 norm of $\boldsymbol{\rho}_{\text{GND}}^{\kappa}$. When accounting for the edge and screw type dislocations in HCP crystals, Eq. (6) is under-defined and the least squares minimization method is applied to solve dislocation densities for all slip systems [36,40].

The dislocation debris relates to the substructure which forms obstacles weaker than the forest dislocations and the strength increase $\tau_{\text{deb}}^{\kappa}$ due to dislocation debris is defined according to the dislocation dynamics studies [42],

$$\tau_{\text{deb}}^{\kappa} = G_{12}k_{\text{deb}}b^{\kappa}\sqrt{\rho_{\text{deb}}^{\kappa}}\ln\left(\frac{1}{b^{\kappa}\sqrt{\rho_{\text{deb}}}}\right) \tag{7}$$

where $\rho_{\text{deb}}^{\kappa}$ is the dislocation debris density, k_{deb} is the material-independent constant determined to be 0.086 [42].

During the load reversal of fatigue tests, dislocation annihilation occurs inside slip systems. Usually a back stress is introduced in this process to incorporate the local reversed stress component due to heterogeneous dislocation distribution and grain interaction. Since the dominant source for generating back stress is not clear in this specific Ti-6242S alloy [43], which could be resulted from the heterogeneity of GND field [44–47], short-range stresses (e.g. reverse dislocation glide from dislocation pile-ups at grain boundaries [27]) or other sources (e.g. dislocation substructure [48]). Here, the reversible dislocation is accounted for now to describe the back stress in the strength hardening rule for capturing the Bauschinger effect, which shows good prediction of heterosis loop [49]. Intrinsically during load reversal, partial stored dislocation is erased and is independent of the dislocation structure formed by the

irreversible forest dislocations [50]. To incorporate the intrinsic dislocation interaction during load reversal, the forest dislocation density are divided into two parts, i.e. forward (irreversible) forest dislocation $\rho_{\mathrm{fwd}}^{\kappa}$ and reversible dislocation $\rho_{\mathrm{rev}}^{\kappa\pm}$ [30,50],

$$\rho_{\mathrm{for}}^{\kappa} = \rho_{\mathrm{fwd}}^{\kappa} + (\rho_{\mathrm{rev}}^{\kappa+} + \rho_{\mathrm{rev}}^{\kappa-}) \tag{8}$$

where $\rho_{\mathrm{rev}}^{\kappa+}$ and $\rho_{\mathrm{rev}}^{\kappa-}$ denote the reversible dislocation density along the loading (κ+) and unloading (κ-) path in each slip system. The governing equations for the evolution of each component in sessile dislocations are introduced in Appendix A.

2.2 Microstructure reconstruction and CP validation

To reconstruct the statistical volume element (SVE) of near-α titanium alloy, the grain information of a near-α Ti-6242S [51] is utilized and its ND (Z) inverse pole figure is shown in Fig 2 (a), where ND, i.e. Z direction, is perpendicular to the loading direction. This near-α Ti-6242S with a duplex annealing process yielding 94% primary α grains ensures no observation of inclusion or precipitates at the micron scale from EBSD [18,51,52]. Tiny beta phase exists only between the primary-α grains and no α lath structure is observed in the microstructure. From previous studies for Ti-6242 microstructure, the ß phase between the α grains barely affects the dislocation slip activated from the primary α grain [53]. The material microstructure therefore could be simplified as polycrystals with equiaxed primary α grains.

Based on the ND EBSD scan applied at the tensile specimen center, software MTEX-5.1.1/MATLAB [54,55] is used to obtain the grain statistics in Fig 2 (b), including the orientation distribution function (ODF), misorientation distribution function (MODF), grain size and grain shape distribution. Grain boundaries are identified using misorientation limit of 4°. The grain statistical distribution functions are incorporated in an open-source reconstruction software, NEPER [56], to generate 100 SVEs shown in Fig 2 (c) with 300 grains per SVE. The calibration of properties in CPFE method is carried out by comparing the stress-strain behavior with experimental tensile data [51] at strain rates of 0.01/s and 1×10^{-4}/s at ambient temperature. It is noted that a variation of stress-strain curves is mainly observed at the strain hardening stage for both strain rates in Fig 2 (d) for the 100 generated SVEs, but all mismatches are within 10% error change which means that all SVEs are satisfied for obtaining reasonable polycrystalline behavior of this near-α Ti-6242S alloy. The one matches best to the experimental data shown in Fig 2 (d) is used as an exemplary SVE in the following investigations and the CP properties are shown in Table 1. A mesh size and type sensitivity study based on the current CPFE framework is provided in Appendix B. Aiming to capture

more accurate local responses at the vicinity of grain boundaries, it which leads to the choice of quadratic hexahedral element (C3D20R) and element size of 0.5 μm.

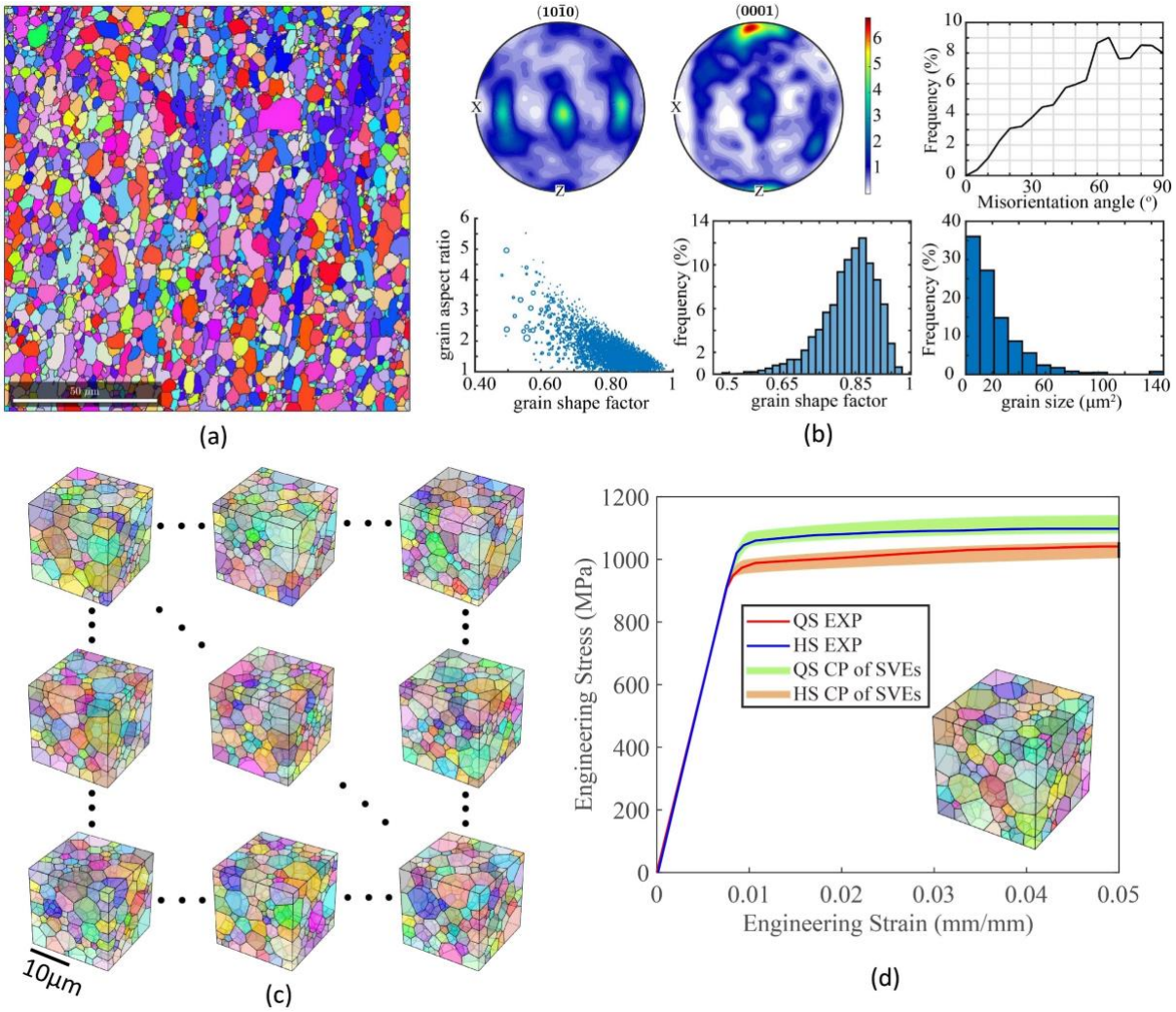

Fig 2 SVE reconstructions. (a) ND (Z) inverse pole figure EBSD map of undeformed specimen; (b) grain statistics including orientation, misorientation, grain size and shape distribution functions; (c) 100 grain statistics satisfying SVEs; (d) Polycrystalline stress-stain behavior in CP compared with experimental data at quasi-static (QS) and higher strain (HS) rates.

Experimental data on single crystals provide very valuable validation information on some of the fundamental properties, linking to manufacturing processes and chemical composition. We contend that the properties could be calibrated and validated with reasonable accuracy based on polycrystalline experimental data as well and the polycrystalline approach was taken here. The Ti-6242S alloy investigated in this study has a microstructure with 94% primary alpha, without any Widdmansttaten, Basketwave or Colony structure [43]. The

reconstructed SVE with equiaxed-grain-only polycrystal is therefore a reasonable representation of the microstructure. The properties that represent the elasto-plastic behaviour of a crystal within the polycrystal microstructure, especially the elastic moduli and CRSS in prism slip system, are consistent with those reported in the literature from single crystal experiments or polycrystalline experiments [57,58]. Thus, the material properties in Table 1 are deemed to capture single-crystal and local grain responses in the material with sufficient accuracy, particularly since the dominant prismatic and basal slip systems are activated with their CRSS values ~2-4 times lower than the ones in pyramidal slip systems [1,59].

3. Fatigue indicator parameters

Multiple fatigue indicator parameters (FIPs) were previously proposed to identify fatigue crack nucleation and predict fatigue lifetimes as a function of the FIPs. In this section, four well established FIPs are incorporated in the consistent CP framework (Section 2). A recently proposed FIP based on dislocation density discrepancy at grain boundaries is validated by comparing with characteristic crystal orientation of fatigue initiation sites from experimental observations. In the following section, it will be compared with other FIPs on their predictabilities over polycrystalline SVEs.

3.1 Established FIPs

Classical Fatemi and Socie FIP was well recognized for predicting fatigue crack nucleation sites upon multi-axial fatigue load [16]. A microscale version of Fatemi-Socie FIP was developed to quantify the driving force for transgranular failure defined based on each octahedral slip system of FCC crystals [60] and for lamellar structure in titanium alloys [61]. The cyclic accumulated plastic strain was proposed as FIP [62,63] to illustrate the observations of nucleated crack lying in the plane of the slip band [64,65]. Stroh [4] established the hard-soft grain pair mechanism for fatigue crack nucleation in near-α titanium alloys where soft-grain dislocation activates and pile-ups at hard-soft grain boundary leading to tensile stress field that initiates crack opening in the hard grain. Mixed-mode crack nucleation FIP [66] was proposed to account for mixed shear and tensile stress in the hard grain and dislocation pile-up length in the soft grain, which was later modified into a nonlocal scheme considering the Nye tensor and GND [3]. Energy-based FID [67] was proposed as a function of dislocation densities and crystal-level stress/strain and its capability was demonstrated to identify crack nucleation sites in experimental observations of HCP and FCC polycrystals [14,68–71].

Table 1 the elastic constants are adopted from previous study at 20 °C [53,72] *and plastic properties are consistent with that from micro-pillar tests* [73].

Crystal property		Units	Quantities (prism)
Elastic	E_1	GPa	84.75
	E_3	GPa	119.79
	G_{13}	GPa	40.00
	ν_{12}		0.46
	ν_{13}		0.32
Plastic	ρ_m	μm^{-2}	5.0
	ν	Hz	1.0×10^{11}
	b	μm	2.94×10^{-4}
	k	$J\cdot K^{-1}$	1.381×10^{-23}
	ΔV	b^3	12
	τ_c^s	MPa	240
	ΔF	J	8.97×10^{-20}

Four of the well-established FIPs are incorporated into the crystal plasticity model described above to investigate the FIP predictions, compared with the proposed FIP (described below) and to compare with the crack nucleation data in experimental observations. Single-crystal experimental observations demonstrate that the accumulated plastic strain is a precursor to fatigue crack initiation, where the initiated crack lies inside the plane of the shear band [74–76]. Here, the accumulated effective plastic strain $\bar{\varepsilon}^p$, as an FIP, is symbolized as R_ε,

$$R_\varepsilon = \bar{\varepsilon}^p = \int_0^t \dot{\bar{\varepsilon}}^p \, dt \tag{9}$$

where $\dot{\bar{\varepsilon}}^p$ is the effective plastic strain rate,

$$\dot{\bar{\varepsilon}}^p = \sqrt{\frac{2}{3}(\dot{\boldsymbol{\varepsilon}}^p : \dot{\boldsymbol{\varepsilon}}^p)} \tag{10}$$

and the plastic strain rate $\dot{\boldsymbol{\varepsilon}}^p$ is a function of the plastic velocity gradient,

$$\dot{\boldsymbol{\varepsilon}}^p = \frac{1}{2}[\mathbf{L}^p + (\mathbf{L}^p)^T] \tag{11}$$

Based on Stroh's theory [4], facet nucleation inside a hard-soft grain pair is a result of dislocation pile-ups and strain accumulation in the soft grain, leading to stress concentration in a neighboring hard grain. Thus, a nonlocal fatigue crack nucleation model was proposed based on a wedge crack nucleation in the hard grain as dislocations pile-up in the soft grain [77]. The nucleation parameter, noted as R_{mix}, is a function of the effective stress T_{eff} and equivalent micro-crack length c on the basal plane [3,4,13],

$$R_{\text{mix}} = T_{\text{eff}} \cdot \sqrt{c} \tag{12}$$

where

$$T_{\text{eff}} = \sqrt{\langle T_n \rangle^2 + \beta T_t^2} \tag{13}$$

$$c = \frac{\mu}{8\pi(1-\nu)\Gamma_s} B^2 \tag{14}$$

T_n and T_t are the normal and shear stress components of a crack plane for mixed-mode crack nucleation. β is the ratio between shear to normal fracture toughness of the material, which is suggested as 0.7071 in [78] for near-α titanium alloy. ν is the Poisson's ratio and Γ_s is the surface energy considered to be 2 J/m^2 for titanium alloys [79]. The crack plane is determined based on the highest mixed-mode stress intensity factor $K_c = T_{\text{eff}}\sqrt{\pi c}$ among all possible planes where dislocations activate and pierce [3]. B is the crack opening displacement, which is assumed equivalent to the displacement pile-up length and calculated as the magnitude of the net Burgers vector **b**. The nonlocal computational scheme solving the net Burgers vector across the reference Burgers circuits [3] is adopted. B is computed from Nye tensor, i.e. curl of plastic deformation gradient $\mathbf{F}^p$, directly correlated with GND in Eq. (6).

The micromechanical interpretation of the Fatemi-Socie model [16] has been applied as FIP to predict the fatigue nucleation sites in aero-engine materials, especially titanium alloys [61,80,81]. It is reported that experimentally observed microstructural crack nucleation sites around an inclusion are not well captured [14], since it lacks crystal-level information, such as localized slip and dislocation densities [16]. A revision to Fatemi-Socie FIP with distinct parameters has been proposed by McDowell [82] to address the correlations between directional plastic strain accumulation and crack formation due to grain or phase boundary dislocation impingement. In this study, the original version of the Fatemi-Socie parameter is implemented as

$$R_{\mathrm{FS}} = \frac{\Delta\gamma^{p}_{\max}}{2}\left(1 + \hat{k}\,\frac{\sigma_{n,\max}}{\sigma_{y}}\right) \tag{15}$$

where $\Delta\gamma^{p}_{\max} = \left(\Delta\varepsilon^{p}_{1} - \Delta\varepsilon^{p}_{3}\right)_{\mathrm{cycle}}$ is the maximum range of cyclic plastic shear strain for each cycle. $\Delta\varepsilon^{p}_{1}$ and $\Delta\varepsilon^{p}_{3}$ are the cyclic increase of maximum and minimum normal plastic strain, respectively. $\sigma_{n,\max}$ is the maximum tensile stress normal to the plane of the maximum shear strain range and σ_y is the uniaxial yield strength. $\hat{k}$ is the parameter controlling the effect of normal stress on fatigue crack formation. The relationship between normal stress and the driving force is not clear, here $\hat{k}$ = 1 is adopted from former R_{FS} implementations in titanium alloys [61,80].

During the cyclic loading process, the energy associated with the plastic deformation may be dissipated or stored within the polycrystalline materials in the form of dislocation structures within the slip bands, dislocation cells or GND that accommodate the local lattice curvature and corresponding plastic strain gradient. It is argued that the density of sessile dislocations and GNDs play an important role in localized stress redistribution causing potential cleavage crack nucleation [15,67]. The microstructural stored energy density is proposed as a mechanistic driver, i.e. FID, as a function of the sessile dislocation and GND, in order to predict fatigue crack nucleation in polycrystal microstructures [67]. The stored energy density is calculated from the total strain energy, which is not dissipated and stored inside dislocation pile-ups and structures, and occupies approximately ξ = 5% of the total plastic work [14]. It is verified to be non-singular [71], which turns out to be a valuable indicator for crack propagation prediction as well. Within the current CPFE framework, the forest and dislocation debris are considered as the main source of the immobile dislocation, and the definition of local stored energy density R_{SED} is modified from original formula [14,15,67],

$$R_{\mathrm{SED}} = \int \frac{\xi\boldsymbol{\sigma}\colon d\boldsymbol{\varepsilon}^{p}}{\sqrt{\rho_{\mathrm{for,tot}} + \rho_{\mathrm{deb,tot}} + \rho_{\mathrm{GND,tot}}}} \tag{16}$$

where $\rho_{\mathrm{for,tot}} = \sum_{\kappa}\rho^{\kappa}_{\mathrm{for}}$, $\rho_{\mathrm{dev,tot}} = \sum_{\kappa}\rho^{\kappa}_{\mathrm{deb}}$, $\rho_{\mathrm{GND,tot}} = \sum_{\kappa}\rho^{\kappa}_{\mathrm{GND}}$.

3.2 FIP based on dislocation density discrepancy

Prior computational investigations of hard-soft grain pairs [3,83] show that the facet nucleation occurs when dislocations pile-up and entangle at the hard-soft grain boundary. In consideration of low dislocation penetration, the accumulation of dislocations under cyclic loading leads to crack nucleation at the hard-soft interface, which propagates across the hard grain, leaving a

penny-shaped facet [3,17]. Recently, this numerical finding was experimentally validated by the transmission electron microscopy (TEM) observations, where dense dislocation networks and dislocation pile-ups are observed near the grain boundary of hard-soft grain pair, mostly inside soft grain after dwell fatigue [26,27]. Shown in Fig 3(a), interestingly near the grain boundary of this grain pair, the dislocation pileups concentrate mostly at the side of soft grain (prismatic) and relatively low dislocation lines in the hard grain (basal). The high dislocation density discrepancy near grain boundary is originated from the slip accumulation in soft grain, and the subsequent slip/dislocation blockage at the hard/soft grain boundary. This potentially leads to high stress concentration during the stress holding period during cruise period of aircraft engine [38,84]. The dislocation based model was firstly proposed by Bache in Fig 3(b) [5] and it was used to model the load shedding phenomenon explicitly shown in real microstructure from recent CP studies in Fig 3(c) [85]. Thus, the observed and validated high discrepancy of dislocation density at hard/soft grain boundaries could be adopted to establish a fatigue indicator parameter FIP for identifying the fatigue facet/crack nucleation. Former works focused on the microstructure effect and uncertainty quantification of this FIP in the reduced order and multi-scale framework [30,32,34,86]. Here it is incorporated in the CPFE framework and studied against other FIPs and experimental observations.

The proposed FIP is a function of the maximum dislocation density discrepancy computed at all grain boundaries within the near-α titanium alloy microstructure, which is noted as MD^3. The total dislocation density in κ^{th} slip system is the summation of sessile dislocation density, including forest and dislocation debris, and the GND density,

$$\rho_{\mathrm{tot}}^{\kappa} = \rho_{\mathrm{for}}^{\kappa} + \rho_{\mathrm{deb}}^{\kappa} + \rho_{\mathrm{GND}}^{\kappa} \tag{17}$$

Explicitly shown in Fig 3(d), MD^3 is computed through the following steps in CPFE:

(1) As shown in Fig 3(d), at current time step of the loading history, the total dislocation density of l^{th} element $[\rho_{\mathrm{tot}}]^l$ is computed as,

$$[\rho_{\mathrm{tot}}]^l = \frac{\sum_h (\rho_{\mathrm{tot}})^h}{H}, \quad (\rho_{\mathrm{tot}})^h = \sum_\kappa (\rho_{\mathrm{tot}}^{\kappa})^h \tag{18}$$

where $(\rho_{\mathrm{tot}})^h$ is the total dislocation density in h^{th} integration point and H is the total number of integration points in the element. $(\rho_{\mathrm{tot}})^h$ is the sum of dislocation densities in all slip systems for this integration point, including basal, prismatic and pyramidal systems. Thus, $[\rho_{\mathrm{tot}}]^l$ is an element -average value of the total dislocation density.

(2) For the i^{th} grain in the microstructure, all the neighbouring grain pairs which share the grain boundaries are in Fig 3(d). The first layer elements adjacent to the grain boundaries are defined as the region of interest, noted as Ω_i for grain i. The element pairs inside region Ω_i are extracted for every element interface, i.e. grain boundaries, the order of which is defined as j. For every element pair in region Ω_i, the maximum dislocation density discrepancy for grain i is defined as,

$$(\Delta\rho_{\text{tot}})^i = \max_{j \in \{1,2,\dots,m_i\}} \left\{ \left| (\Delta\rho_{\text{tot}})^j \right| \right\} \tag{19}$$

where m_i is the total number of element pairs in region Ω_i.

Then, the proposed FIP R_{MD3}, the MD^3, is computed as,

$$R_{\text{MD3}} = \Delta\rho_{\text{tot}} = \max_{i \in \{1,2,\dots,n\}} \left\{ (\Delta\rho_{\text{tot}})^i \right\} \tag{20}$$

where n is the total number of grains in the microstructure.

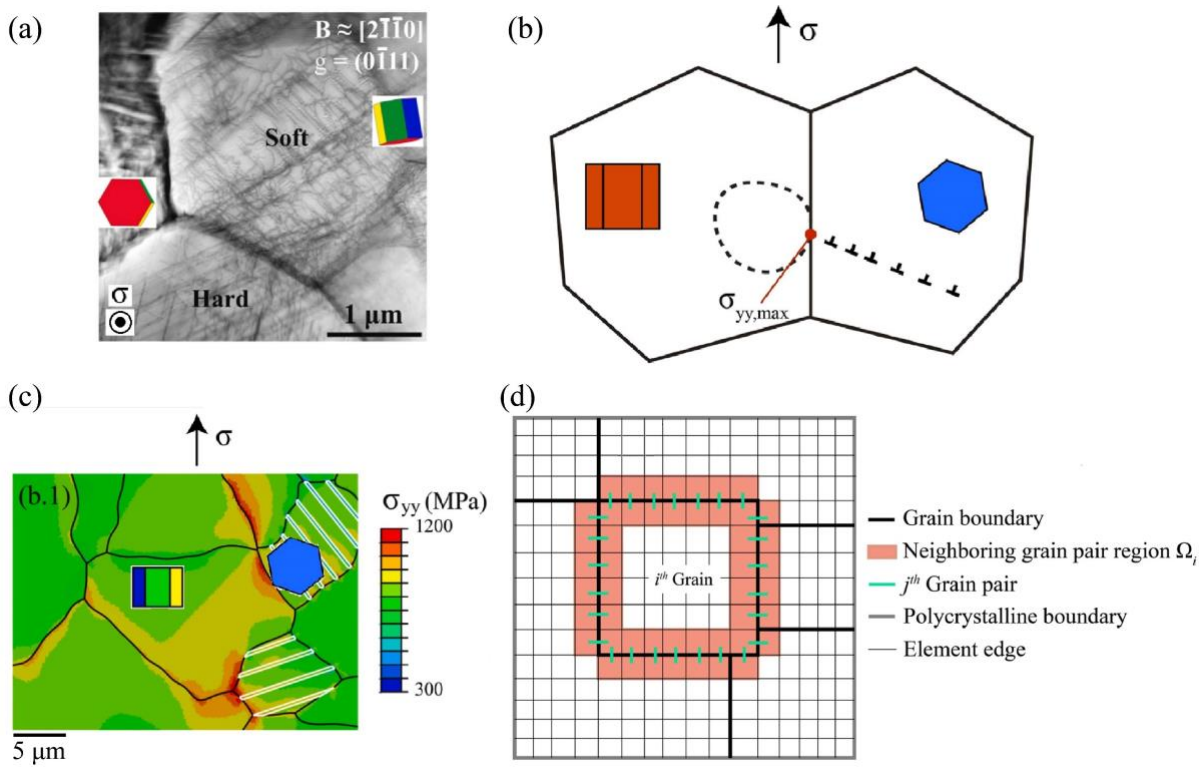

Fig 3 Origin of FIP solely based on dislocation density discrepancy, including (a) high dislocation pile-up and discrepancy observed at hard/soft grain pair in near-α Ti6242Si [26]*; (b) adapted Bache's model explains the slip accumulation in soft grain and resulting stress concentration in hard grain* [5]*; (c) load shedding phenomenon leads to high stress concentration in hard grain in CP model* [85]*; (d)*

the proposed MD^3 computed in CPFE framework to identify crack nucleation site for all grain boundaries.

3.3 Bi-crystal validation of MD^3

Former experimental observations show that specific crystallographic ranges are extracted for the facet/crack nucleation sites upon both pure (none dwell) and dwell fatigue cases [7,8,10–13]. To investigate the validity of the current fatigue indicator parameter MD^3 of capturing experimental data, two typical pure and dwell fatigue loading conditions are investigated in Fig 4 (a,b). These loading conditions are chosen due to their wide usage in general coupon test at stress level of ~95% yielding stress σ_Y [7,11,12], leading to the summarised experimental crystallographic data shown in Fig. 1. It is recently reported that the time for local peak stress to reach equilibrium in equiaxed microstructure is between 50-66s [87], and the 2 min dwell would allow stress equilibrium while the load shedding takes place during stress hold. Frequency effect has been studied for near-alpha titanium under cyclic loading, and the higher frequencies produce higher maximum stress existing in the material, leading to shorter lifetimes [88]. In a dwell fatigue test, the decrease of load up rate enables more plastic deformation established during load up stage, thus less load shedding during the load hold [87].

Stress, strain or FIPs were observed to stabilize after 3-10 cycles during pure or dwell fatigue loads [20,89,90], and cycle number of 50 is chosen here to obtain fully saturated or stabilized FIPs for both loading conditions in Fig 4 (a,b). Fig 4(c) shows two neighbouring grains, A and B, in the middle of exemplary SVE from calibration in Fig 2(d). Boundary conditions in Fig 4 (c) are set, such that polycrystalline behaviour is subjected to uniaxial fatigue load in a coupon test. To focus on the dislocation density evolution and eliminate grain interaction effect of other grains adjacent to grain A or B, mechanical behaviour in the SVE region outside A/B grain pair is idealized using bi-linear elasto-plastic model. It yields at 1030 MPa at 0.2% strain and the tensile stress reaches 1120 MPa at 9% strain, representative of the uniaxial tensile data of Ti-6242S at room temperature [51]. CP model is used in grains A and B. It is assumed that crack nucleates between grain A and B and MD^3 is extracted at A/B boundary for different A/B orientation combinations.

In the top-down view of Fig 4(d), path P-Q is perpendicular to the boundary of grains A and B. The crystal orientations of grain A and B are set in plane PQZ. In Fig 4(e), the mismatch angles are changed by rotating the c-axes of grain A and B in the PQZ plane. To avoid forming same crystallography, the rotating direction is clockwise for B and

counterclockwise for A. MD^3 is only extracted at region near grain boundaries as explained in Fig 3 (d). It is worth noting that these two grains are chosen such that their relative length ratios is less than 0.25. Choosing a larger grain pair would lead to altering the polycrystalline behaviour while changing their orientations, which in-turn change the responses significantly near their grain boundary. A convergence study of the relative length ratio between grain pair and SVE is conducted in Appendix C, leading to current choice of 0.143 (valid when <~0.2).

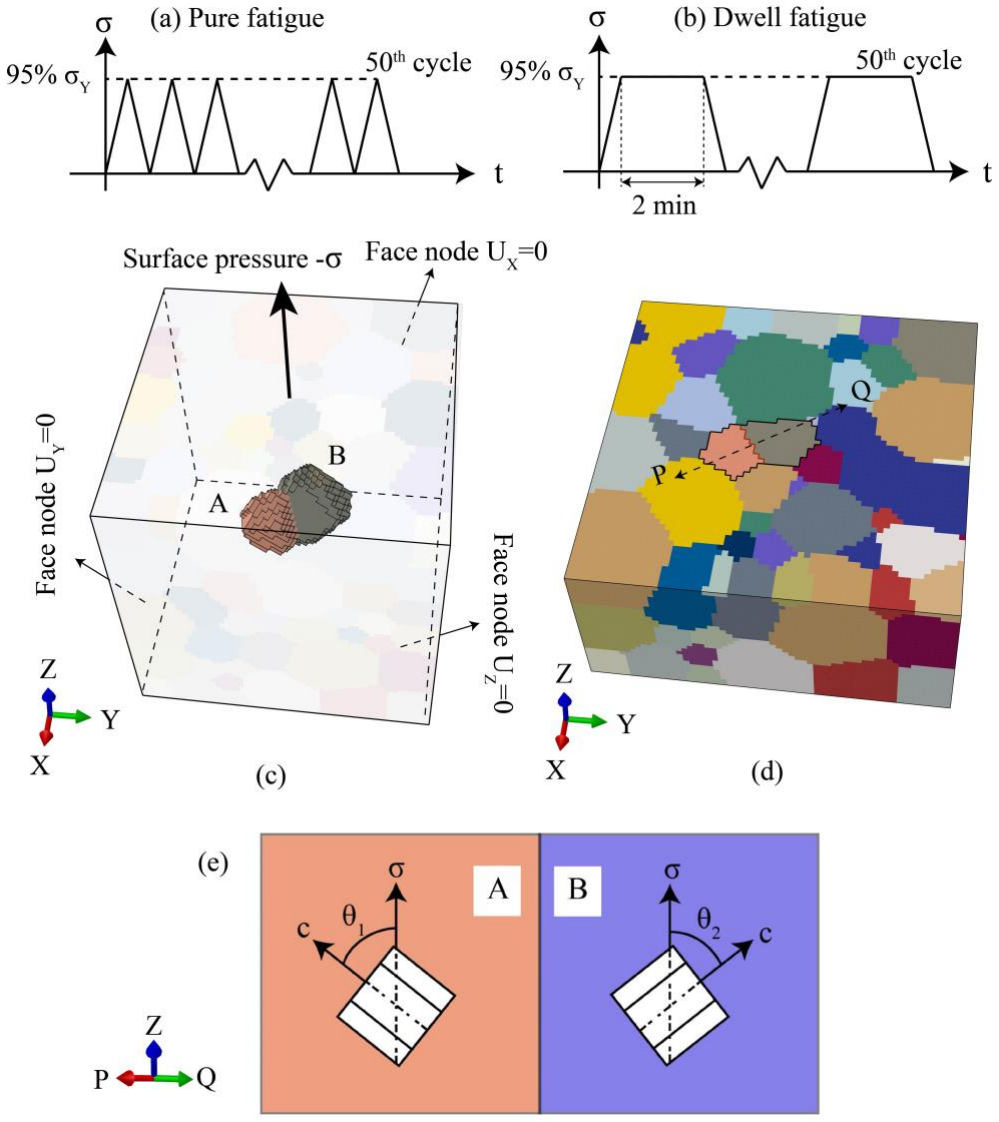

Fig 4 Grain pair study for fatigue indicator parameter MD^3 including loading condition for (a) pure fatigue and (b) dwell fatigue, (c) grain pair chosen in exemplary SVE, (d) sub-view in Z plane, (e) grain orientation set-up for grain A and grain B.

As crystallographic configurations of the grain pair changes, MD^3 between grains A and B varies with the mismatch angles of grain A (θ_1) and B (θ_2). The trends of MD^3 are plotted as a function of θ_1 and θ_2 subjected to fatigue and dwell fatigue conditions in Fig 5. The plotted

values correspond to the peak load at the 50th cycle. In both pure and dwell fatigue conditions (Fig 5 (a) and (b)), MD^3 shows a symmetric shape profile and the similar θ_1 and θ_2 angles lead to a lower level of MD^3 magnitudes, due to a 'mirrored' dislocation density distribution in the grain pair. This results from similar slip activation and corresponding resolved shear stress when similar mismatch angles are chosen with respect to the loading direction. As the difference between angle θ_1 and θ_2 gets larger, less dislocations are activated within harder grain (with small θ_1 or θ_2) whereas more dislocations generate in softer grain (with large θ_1 or θ_2), leading to the increase in MD^3.

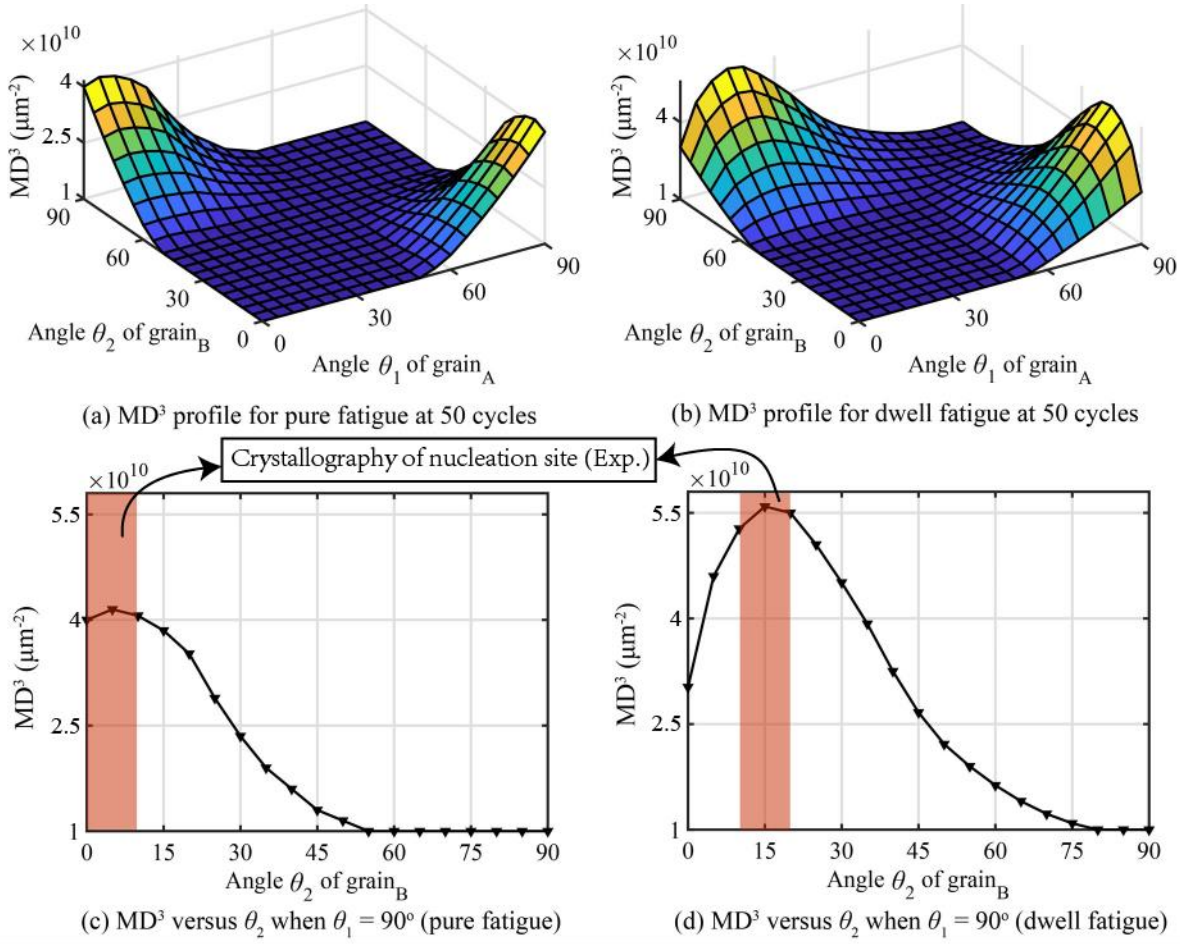

Fig 5 the MD^3 profiles change with mismatch angles of grain A and grain B, θ_1 and θ_2 under (a) pure fatigue and (b) dwell fatigue load. The MD^3 profile sections are shown when the grain A becomes a soft grain, i.e. $\theta_1 = 90^o$, under (c) pure fatigue and (d) dwell fatigue loading conditions. The shaded regions in (c) and (d) indicate experimental observations.

3.4 FIPs distribution in a worst-case scenario

It has been known from various CP and experimental studies that the worst-case scenario for fatigue crack to nucleate in bulk material is a hard-soft grain pair configuration

[5,10,20,83,85,91–93], for near-α titanium alloys. Here, all FIPs introduced are assessed in the worst-case scenario, to understand the distribution patterns of the FIPs and their linkage to fatigue crack nucleation. Critical hard/soft grain pair A/B is embedded in the exemplary SVE shown in Fig 4 (c), with grain pair modelled by CP and the remaining by elasto-plastic model introduced in former section. The pure and dwell fatigue loads and boundary conditions are set the same as shown in Fig 4 (a-c), and the distribution pattern of FIPs are extracted along path P-Q in Fig 4 (d). Grain A is set to be hard and grain B is soft, where c-axis of A is pointing towards load direction Z and c-axis of B is parallel to XOY plane and perpendicular to path P-Q. The FIPs are normalized by their maximum value and plotted along the path P-Q perpendicular to the grain boundary in Fig 6 for both pure and dwell fatigue loads at 50^{th} load cycle. Mesh sensitivity has been conducted for the location and values of different FIPs, shown in Appendix B.

FIP R_ε is high inside the soft grain and much lower in the hard grain, showing significant strain partitioning at grain boundary. This resulted from the easiest activation of prismatic slip and corresponding accumulated plastic strain in soft grain, whereas the slip in hard grain was barely activated under the same remote stress load. Higher strain accumulation and R_ε is observed in the dwell fatigue case due to creep plastic strain increase during each load holding period of dwell fatigue cycles.

Fatemi-Socie parameter R_{FS} shows a drop from soft to hard grain at the grain boundary and a higher drop is observed upon dwell fatigue load. The drop is mainly linked to maximum shear strain range $\Delta\gamma^p_{\max}$ since prismatic slip accumulation is high in the soft grain, whereas barely any slip activation observed in the hard grain. The maximum tensile stress $\sigma_{n,\max}$ perpendicular to the maximum shear strain plane is a bit lower in the soft grain, compared with that in the hard grain, since $\sigma_{n,\max}$ direction is close to the c-axis and its value is close to the yielding stress σ_y in the hard grain. However, the contribution of $\Delta\gamma^p_{\max}$ is dominant in R_{FS}, compared with $\sigma_{n,\max}$ which is normalized by the yielding stress σ_y and the drop of R_{FS} at grain boundary is mainly controlled by the local shear strain accumulation, i.e. slip accumulation in major prismatic slip system. R_{FS} shows similar trend as R_ε, both majorly dependent on the slip activation.

Since R_{MD3} is only computed near grain boundary elements shown in Fig 3, to visualized R_{MD3}, total dislocation density ρ_{tot} (Eq.10) instead of $\Delta\rho_{\mathrm{tot}}$ (Eq.11) is plotted through path P-Q to show the local dislocation density distribution. A high level of dislocation

density discrepancy is observed at the grain boundary upon pure fatigue load, which equals to large MD^3 at the hard-soft interface. The higher level of dislocation density in soft grain results from the predominant prism slip activation, accumulation, and strain hardening behavior, which in-turn further pushes up the local stresses and pinning dislocation densities. Basically, GND increases due to the local intense lattice curvature changes, and SSD increases with shear slip strain accumulation. Whereas in the hard grain, nearly no dislocation accumulation is involved, leaving nearly the initial dislocation density. It should be noted that the reducing rate of dislocation recovery/annihilation ρ_{rev} during load reversal could not catch up with the increasing rate of forward dislocation ρ_{fwd}. Higher discrepancy of dislocation density is observed under the dwell fatigue in Fig 6 (b) due to creep plasticity allowing more prismatic slip activation during the stress hold, which is consistent with prior discrete dislocation plasticity (DDP) and CP studies [20,91].

The mixed-mode cracking FIP R_{Mix} shows a different distribution pattern from the former ones of R_{ε}, R_{FS}, ρ_{tot}. Much higher magnitude of R_{Mix} is observed in the hard grain opposite to the soft one. This results from the mixed mode effective stress T_{eff}, which is much higher in hard grain than that in the soft grain, mainly due to elastic anisotropy where c-axis has higher modulus. Besides, the crack length c is computed from the Nye tensor [3], i.e. GND accumulation, and plastic strain gradient from neighboring grain, which is higher in the hard grain compared with that in the soft grain. Thus, both higher magnitudes of T_{eff} and c lead to even higher R_{Mix} in the hard grain, which has the most potential to initiate facet nucleation. R_{Mix} is higher in the dwell fatigue since stress increases in hard grain and creep strain accumulates in soft grain, i.e. higher GND accumulation and crack length c, due to load shedding mechanism [2,94].

Instead of showing high discrepancy between hard/soft grains in former distributions (R_{ε}, R_{FS}, ρ_{tot}, R_{Mix}), the stored energy FIP R_{SED} is high at the grain boundary for both hard and soft grains, but not specifically in one grain. R_{SED} is proposed based on the deformation energy stored in the dislocation structure, where both stress and strain components are considered. The pinning of dislocations including SSD and GND leads to less mean free path ($l = 1/\sqrt{\rho_{\mathrm{tot}}}$) for dislocation mobility which lower the R_{SED}. Therefore, high R_{SED} in soft grain comes from the intense prismatic slip accumulation and high R_{SED} in hard grain results from the relatively higher stresses in the hard grain (elastic anisotropy) and higher mean free path with lower GND density accumulation. R_{SED} is expected to increase upon dwell fatigue load since slip

accumulation in soft grain and stress increase in hard grain will be strengthened during load shedding phenomenon.

Overall, all FIPs studied in this paper show significantly higher magnitude at the grain boundary, either in soft, hard or both grains. And their drops/increases at the hard/soft grain boundary are enhanced in dwell fatigue case due to load shedding phenomenon. This demonstrates their capability of capturing this worst-case scenario during pure and dwell fatigue loads.

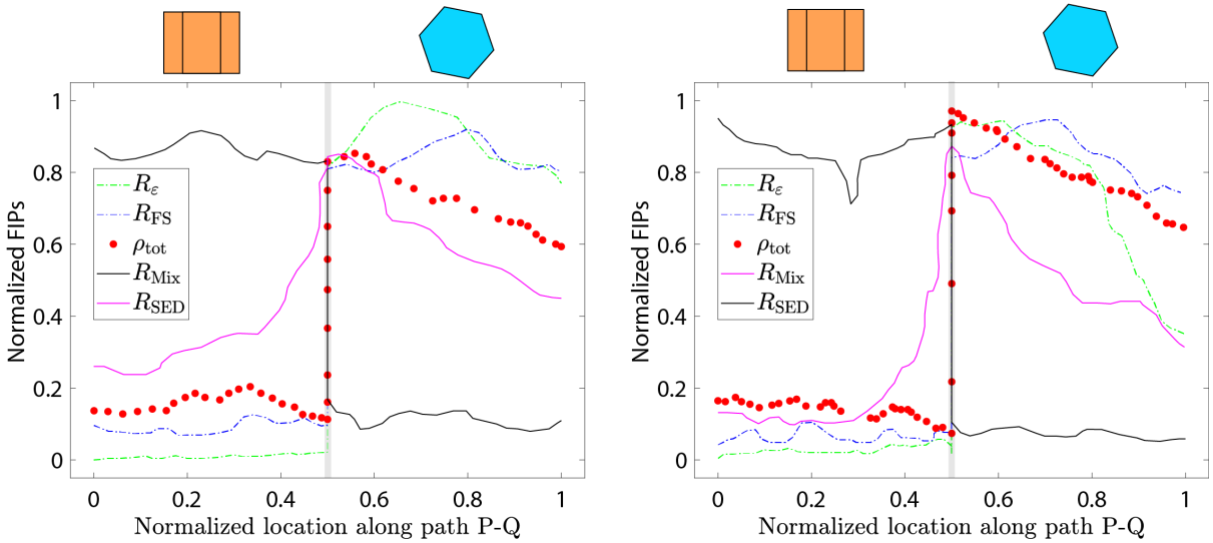

Fig 6 FIPs distribution along path P-Q across the A/B (hard/soft) grain pair for (a) pure fatigue and (b) dwell fatigue at the 50th cycle.

4. Polycrystalline SVE statistical comparison for FIPs

Grain pair embedded in polycrystal is studied to show the direct linkage of proposed MD^3 to worst-case orientations in experimental observations. A worst-case hard/soft grain pair is captured by all FIPs, and their unique mechanisms are illustrated accordingly. Polycrystalline fatigue crack nucleation is much more complex since various orientation combinations and grain morphologies are involved. Various SVEs are studied in this section to compare characteristics of fatigue crack nucleation sites for all FIPs.

4.1 Correlation of nucleation site distances

In current section, CPFE simulations of polycrystalline SVEs were performed using the same boundary and load conditions introduced in Fig 4. The critical nucleation site of each FIP is extracted and defined as the one where the highest FIP magnitude R_η (η=ε, MD3, Mix, SED

and FS) is observed. For all 100 validated SVEs from Fig 2, it is observed that critical sites are mostly at or near grain boundaries of relative 'hard' and 'soft' grain pairs. To compare the nucleation site location from different FIPs in one SVE, the critical site predicted by R_{MD3} is chosen as the reference site. The distances between nucleation site from R_{MD3} and the ones from other FIPs are extracted as shown in Fig 7. After testing 100 validated SVEs upon one loading condition, it leads to 4 distance collections with 100 elements in each collection, i.e. DR_η (η =ε, Mix, SED and FS) in Fig 7.

To understand the statistical correlation of the distance collections from different FIPs, Pearson's correlation coefficient (PCC) $r(DR_\eta, DR_\lambda)$ is computed between DR_η and DR_λ (η or λ=ε, Mixed, SED and FS),

$$r(DR_\eta, DR_\lambda) = \frac{\mathrm{cov}(DR_\eta, DR_\lambda)}{\varsigma(DR_\eta)\varsigma(DR\lambda)} \tag{21}$$

where cov is the covariance function and ς is the expectation function. The correlation between DR_η and DR_λ is plotted for each SVE (as one point), and the correlation distributions are plotted for all SVEs, shown in Fig 8 and 9 for pure and dwell fatigue loads, respectively. In the case of $\eta = \lambda$, the normalised distribution is shown for only DR_η (η =ε, Mix, SED and FS).

In the pure fatigue case shown in Fig 8, elements inside both collection DR_{SED} and DR_{Mix} are all inside the range of 0 to 2.5 μm and have over 85% possibility of distance less than 1.5 μm, which is significantly less than the average grain size of 3 μm. This demonstrates that critical nucleation sites predicted by R_{SED} and R_{Mix} are quite close to that by R_{MD3}, within distance of certain grain diameter. Besides, the interesting find is that DR_{SED} and DR_{Mix} have a reliable correlation with PCC factor of 0.97, which means that the critical sites of R_{SED} and R_{Mix} are potentially the same or similar locations adjacent to each other.

DR_ε is inside range of 0 to 6 μm and with 22% of > 3 μm (average grain size) where these sites show a relatively long distance between R_ε and R_{MD3}. A sparser distribution is shown in the correlation map between DR_ε and DR_{SED} (DR_{Mix}) and their PCC factor is only 0.61 (0.61), which means sites predicted by R_ε are away from those from DR_ε and DR_{SED}. DR_{FS} has even longer distance from R_{MD3}, ranging from 0 to 15 μm and 33% possibility of > 3 μm, and worse PCC factors of 0.31, 0.49, 0.47 with DR_ε, DR_{SED} and DR_{Mix}. This basically means that sites predicted by R_{FS} are significantly away from the ones by R_{MD3}, R_ε, R_{SED} and R_{Mix}.

In the dwell fatigue case in Fig 9, elements inside both collection DR_{SED} and DR_{Mix} remain inside the range of 0 to 2.5 µm which demonstrates a close distance between R_{MD3} sites and R_{SED}/R_{Mix} sites. The correlation between the DR_{SED} and DR_{Mix} is slightly increased to 0.98 and this means the predicted critical sites of R_{SED} and R_{Mix} have more potential to be the same location under dwell fatigue However, the distance possibility of > 3 µm (average grain size) increases to 25% and 36% for DR_{ε} and DR_{FS}, showing a longer distance from the critical sites of R_{MD3}. And their PCC factors with other DR_{η} collections decrease, which means less correlation is observed for R_{ε} and R_{FS} sites with ones from other FIPs.

For the 100 SVEs studied under pure and dwell fatigue load, the critical sites predicted by R_{SED} and R_{Mix} are mainly adjacent to each other, and they are both close to the ones predicted by R_{MD3} with over 85% possibility of less than 1.5 µm, half of average grain diameter. Over 20% (30%) critical sites of R_{ε} (R_{FS}) are away from R_{MD3} with distance more than average grain diameter. Moderate correlation is observed between R_{ε} sites and R_{SED} as well as R_{Mix}, whereas negligible correlation is observed between R_{FS} sites and ones predicted by other FIPs.

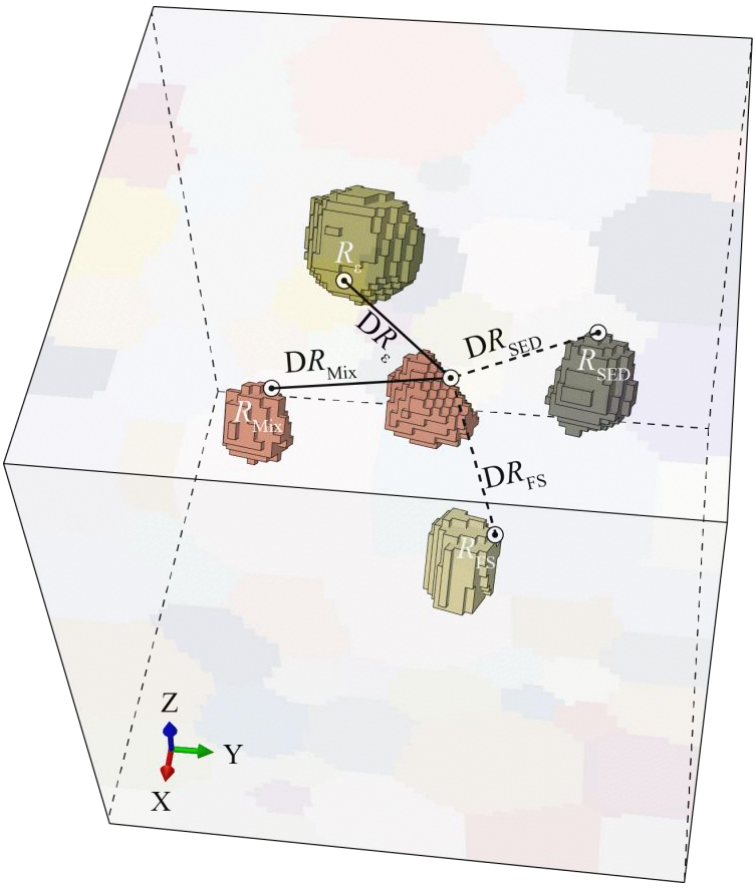

Fig 7 Schematic definition of distances between nucleation sites of proposed FIP (MD^3) and other FIPs.

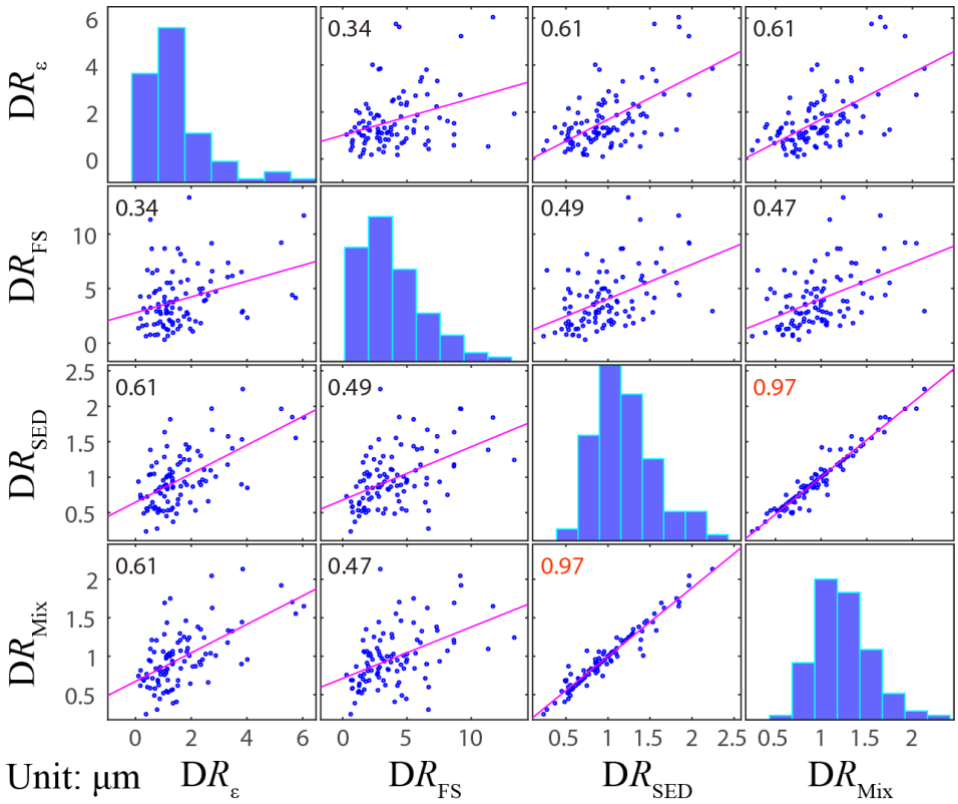

Fig 8 Correlation coefficients between DR_η and DR_λ (η or λ=ε, Mix, SED and FS). If $\eta = \lambda$, the normalized histogram is shown for DR_η. 100 SVEs are tested upon pure fatigue load.

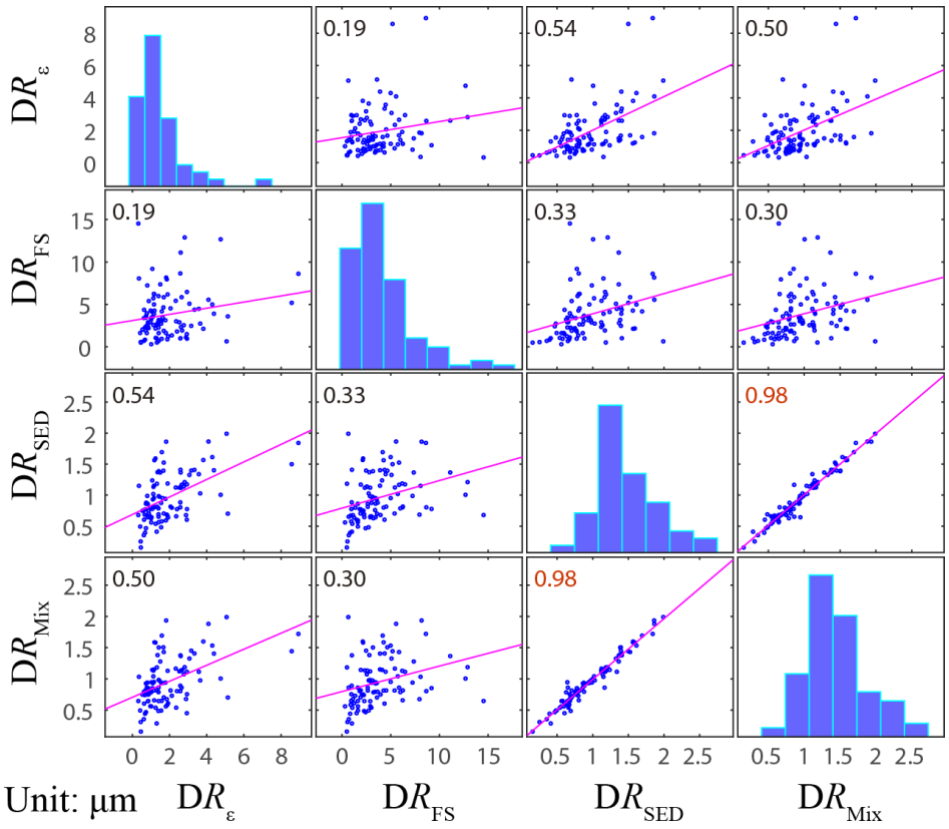

Fig 9 Correlation coefficients between DR_η and DR_λ (η or λ=ε, Mix, SED and FS). If $\eta = \lambda$, the normalized histogram is shown for DR_η. 100 SVEs are tested upon dwell fatigue load.

4.2 Characteristic grain orientations of initiation site

In this section, the orientation characteristics are investigated for the fatigue crack initiation site. Experiments and CP studies have shown that the orientation of facet initiation site is hard or relatively hard for both pure and dwell fatigue load cases [5,10,20,83,85,91–93]. A slight orientation range shift is observed from pure to dwell fatigue cases, which has been introduced in Fig 1. Here, the 'harder' grains are presumed as potential initiation sites, defined as those with small mismatch angles $\theta < 60^o$ between c-axis direction c and loading direction $l = [0\ 0\ 1]^T$, i.e. $\theta = \text{acos}\,[(\mathbf{c}\cdot\mathbf{l})/(|\mathbf{c}|\cdot|\mathbf{l}|)]$. It has been observed in CP studies that critical sites are mostly at or near grain boundaries of relative 'hard' and 'soft' grain pairs, and the hardest grain near maximum value of R_η (η=ε, MD3, Mix, SED and FS) is identified as the fatigue initiation site with its individual grain orientation plotted in (0001) pole figure (PF) in Fig 10 and its orientation distribution function plotted in inverse pole figure Z (IPFZ) in Fig 11. (0001) PF and IPFZ are plotted for dwell fatigue load in Fig 12 and 13.

In the pole figure, Fig 10 shows a spread-out distribution of initiation site orientations for R_ε and R_{FS}. Some critical sites have mismatch angles θ close to 45º, which are confirmed to be surrounded by softer grains with higher mismatch angles ~ 90º. Even if these critical sites are not hard enough with mismatch angle of ~45º, apparently prismatic slip systems are easily activated in their surrounding softer grains to increase high slip localization, and hard-soft grain pair combination is not necessarily needed in these cases to reach high R_ε and R_{FS}, which are mainly controlled by local slip as discussed in Section 3.4. R_ε and R_{FS} show certain grains in the mismatch angle range $\theta < 10^o$, which is less dominant, whereas R_{MD3}, R_{SED} and R_{Mix} clearly shows their dominant orientation inside the mismatch angle range θ less than ~10º. In the IPFZ, Fig 11 explicitly shows the mismatch angle θ range [0, 33º] for R_ε, [0, 45º] for R_{FS}, and [0, 11º] for R_{MD3}, R_{SED} and R_{Mix}, where the dominant θ range is between [10º, 20º] for both R_ε and R_{FS}. A gradient is shown in case of R_{MD3}, R_{SED} and R_{Mix} where 'harder' grain has higher density up to 120 in IPFZ, which means that 'harder' grain has higher potential to initiation crack upon pure fatigue load. This is consistent with experimental observation in Fig 11(f) where more crack nucleation sites are observed in lower mismatch angle θ and mainly distributed within range of [0º, 8º] [7,11,12].

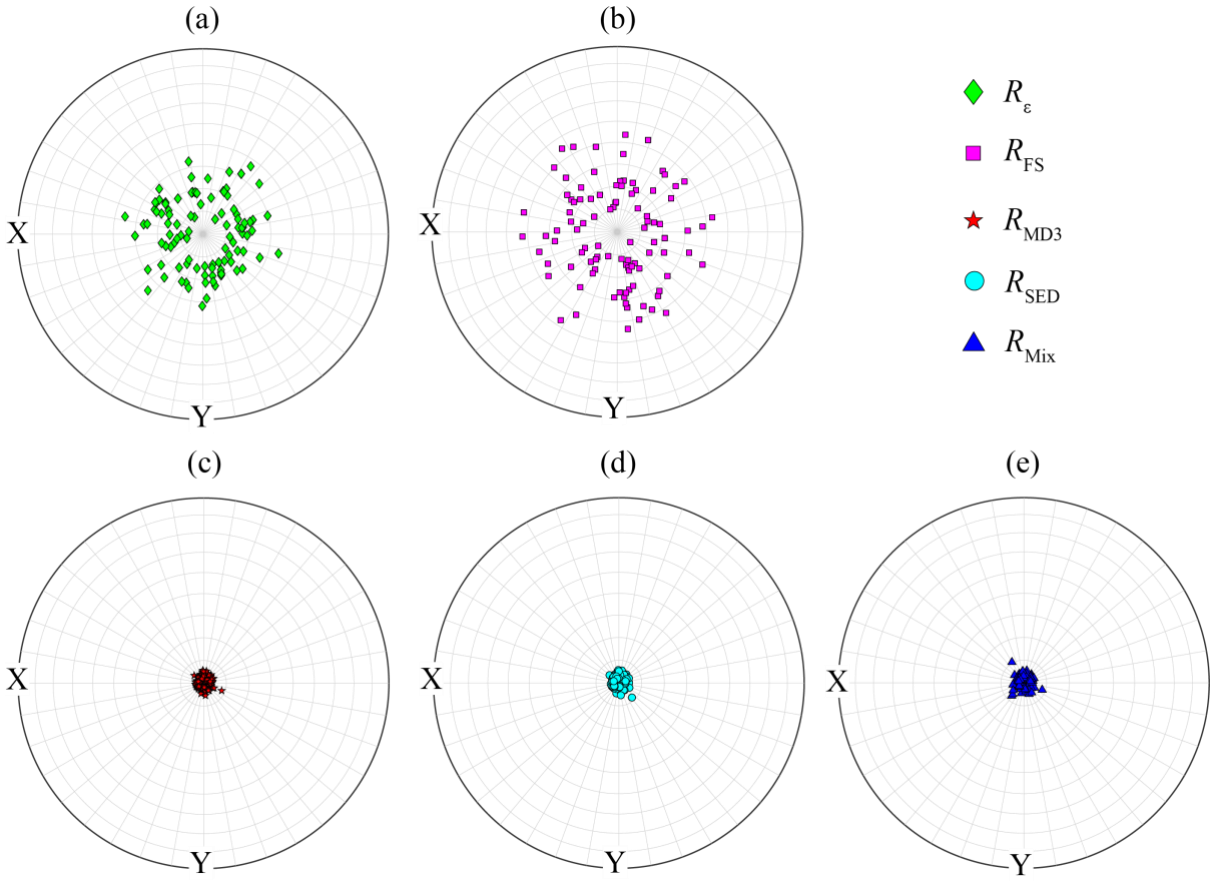

Fig 10 Individual orientations of crack nucleation sites in (0001) pole figure from 100 SVEs for (a) R_ε, (b) R_{FS}, (c) R_{MD3}, (d) R_{SED}, (e) R_{Mix}, upon pure fatigue.

Upon dwell fatigue load, PF in Fig 12 shows a similar scatter pattern for R_ε and R_{FS} with no critical nucleation sites within mismatch angle <10°, whereas some nucleation sites are still existing within this range for R_{MD3}, R_{SED} and R_{Mix} with a clear 'ring' patterns of orientations observed. Dominant mismatch angle θ switches to anther range with higher angles for all FIPs in the IPF within Fig 13, [17°, 30°] for R_ε, [18°, 35°] for R_{FS}, and [10°, 15°] for R_{MD3}, R_{SED} and R_{Mix}. The mismatch angle from experimental observation in Fig 13(f) shows a range of ~[10°, 20°]. It is interesting to see the predicted mismatch orientation region is inside the experimental measurement where the fatigue nucleation sites from CP validated SVEs has no bias and is loyal to the Ti-6242S microstructure reconstructed, compared with crystallographic orientation measurement from initiated facet [10,95]. This is consistent with former probabilistic fatigue crack nucleation model based on R_{Mix} showing a dominant mismatch angle rangle of ~[10°, 30°], which is within the experimental measurement range for Ti-7Al [13]. Though R_ε and R_{FS} do not directly capture the facet nucleation sites, they are consistent with a recent study shows a slip trace orientation within range of ~ [10°, 35°] for Ti-6242 at room temperature [96], which

demonstrates their capability of capturing slip localization sites [7,13]. In bi-modal microstructures with both equiaxed and colony grains, more scattering data was observed for the spatial orientations of crack/facet initiation and neighboring facets in both cyclic and dwell fatigue of titanium alloys, including Ti-6242S alloy [97] and other duplex titanium alloys [98–100], which might be better predicted by the variability of R_ε and R_{FS}. It is also noted that the microstructure investigated in this manuscript contains only equiaxed grains from EBSD scan [43]. This could be the reason for less scattered data observed for the former investigated fractography data [7,11–13].

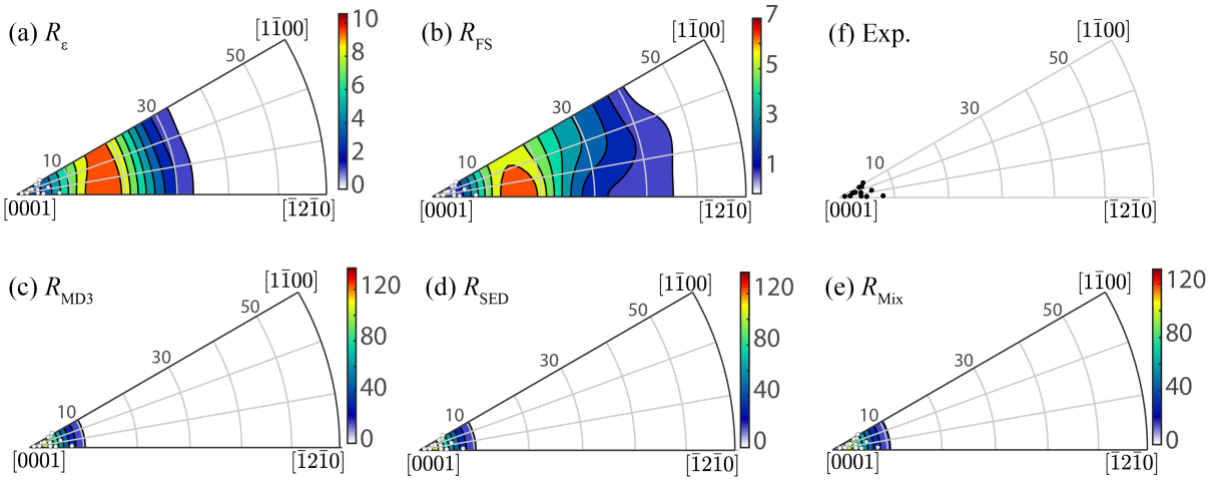

Fig 11 Orientation distribution function of crack nucleation sites in IPFZ from 100 SVEs for (a) R_ε, (b) R_{FS}, (c) R_{MD3}, (d) R_{SED}, (e) R_{Mix} upon pure fatigue, and (f) experimental data from Fig 1(c). Experimental data are also plotted in Figs. (a-e) to show explicit comparison.

5. Conclusion

In this paper, we conduct a comparative study on different fatigue indicator parameters (FIPs) for near-α titanium alloys, including several well-established FIPs and a recently proposed one from our previous work, i.e., R_{MD3}, solely based on dislocation density. All FIPs are implemented in the same crystal plasticity framework based on sessile dislocation reversal and geometrically necessary dislocation for one-to-one comparison. The proposed R_{MD3} is found directly linking to the experimental worst-case orientation ranges in a bi-crystal study. A hard/soft grain pair scenario embedded in exemplary SVE shows the critical sites of FIPs are all near grain boundaries. Upon multiple validated SVEs, distances among different fatigue nucleation sites and crystal orientations of the sites are studied for all FIPs. Under both pure and dwell fatigue loads, short distances and reliable correlations are observed among nucleation sites of R_{MD3}, R_{SED} and R_{Mix}, whereas R_ε and R_{FS} nucleation sites are a bit away. Crystal

orientations of R_{MD3}, R_{SED} and R_{Mix} sites satisfy the experimentally measured mismatch angle range and the range shift from pure to dwell fatigue. R_{ε} and R_{FS} are inclined to capture the orientation range of slip localization from independent slip trace data in Ti-6242.

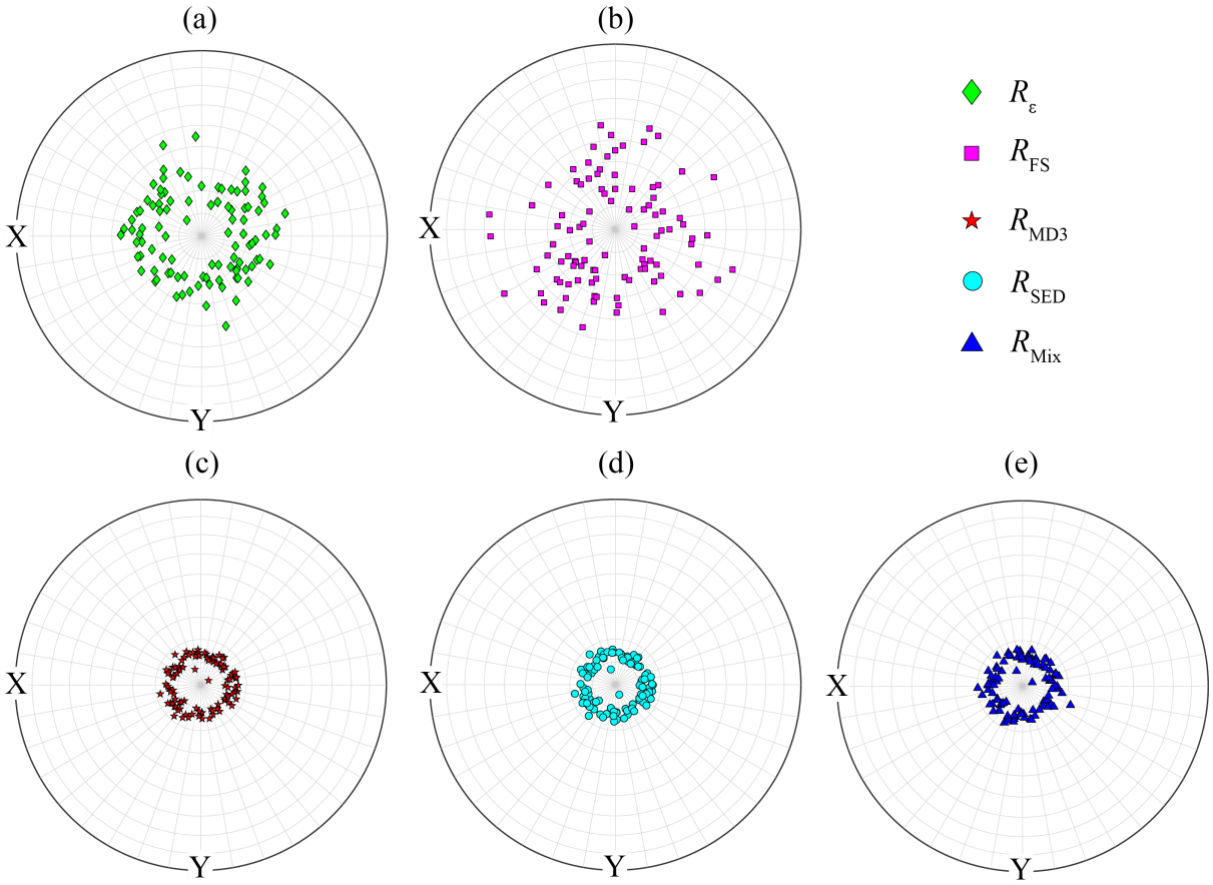

Fig 12 Individual orientations of crack nucleation sites in (0001) pole figure from 100 SVEs for (a) R_{ε}, (b) R_{FS}, (c) R_{MD3}, (d) R_{SED}, (e) R_{Mix}, upon dwell fatigue.

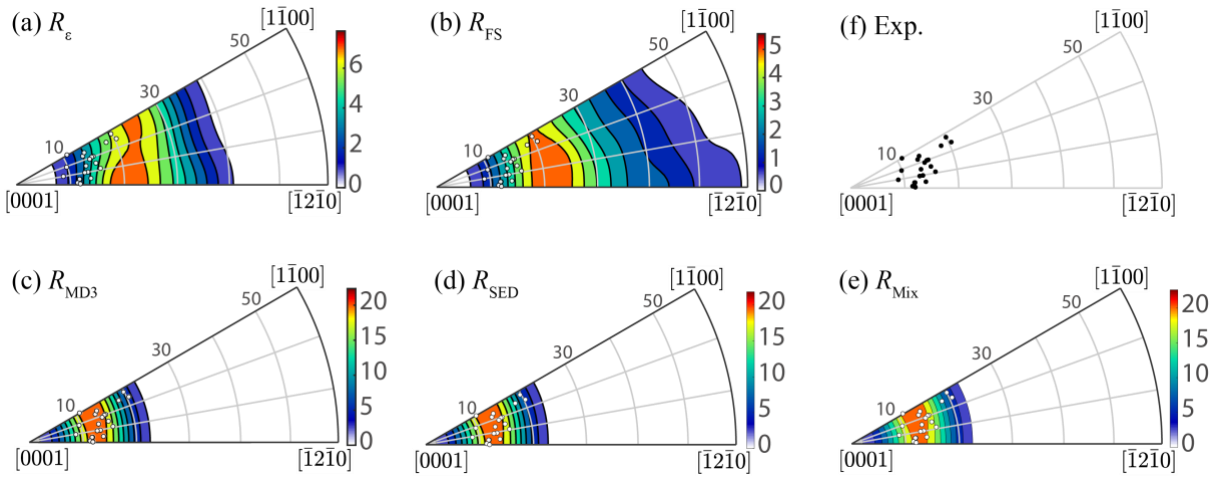

Fig 13 Orientation distribution function of crack nucleation sites in IPFZ from 100 SVEs for (a) R_{ε}, (b) R_{FS}, (c) R_{MD3}, (d) R_{SED}, (e) R_{Mix} upon pure fatigue, and (f) experimental data from Fig 1(d). Experimental data are plotted in Figs. (a-e) to show explicit comparison.

Acknowledgements

The authors gratefully acknowledge the financial support of Air Force Office of Scientific Research (Grant No. FA 9550-13-1-0104) and NASA ESI Program (Grant No. 80NSSC20K0294) and the National Science Foundation provided through the IR/D program. Additional support provided to XZ by the start-up funding from the University of Wyoming is also greatly acknowledged. The authors would like to thank Professor Fionn P.E. Dunne (Imperial College London) for granting access to their code and their helpful suggestions in the preparation of the manuscript.

Reference:

[1] Hasija V, Ghosh S, Mills MJ, Joseph DS. Deformation and creep modeling in polycrystalline Ti-6Al alloys. Acta Mater 2003;51:4533–49. https://doi.org/10.1016/S1359-6454(03)00289-1.

[2] Dunne FPE, Rugg D, Walker A. Lengthscale-dependent, elastically anisotropic, physically-based hcp crystal plasticity: Application to cold-dwell fatigue in Ti alloys. Int J Plast 2007;23:1061–83. https://doi.org/10.1016/j.ijplas.2006.10.013.

[3] Anahid M, Samal MK, Ghosh S. Dwell fatigue crack nucleation model based on crystal plasticity finite element simulations of polycrystalline titanium alloys. J Mech Phys Solids 2011;59:2157–76. https://doi.org/10.1016/j.jmps.2011.05.003.

[4] Stroh AN. The formation of cracks as a result of plastic flow. Proc R Soc Lond A Math Phys Sci 1954;223:404–14. https://doi.org/10.1098/rspa.1954.0124.

[5] Bache MR. A review of dwell sensitive fatigue in titanium alloys: The role of microstructure, texture and operating conditions. Int J Fatigue 2003;25:1079–87. https://doi.org/10.1016/S0142-1123(03)00145-2.

[6] Sinha V, Mills MJ, Williams JC. Understanding the contributions of normal-fatigue and static loading to the dwell fatigue in a near-alpha titanium alloy. Metallurgical and Materials Transactions A 2004;35:3141–8. https://doi.org/10.1007/s11661-004-0058-z.

[7] Sinha V, Mills MJ, Williams JC. Crystallography of fracture facets in a near-alpha titanium alloy. Metall Mater Trans A Phys Metall Mater Sci 2006;37:2015–26. https://doi.org/10.1007/s11661-006-0144-5.

[8] Sinha V, Spowart JE, Mills MJ, Williams JC. Observations on the faceted initiation site in the dwell-fatigue tested Ti-6242 alloy: Crystallographic orientation and size effects. Metall Mater Trans A Phys Metall Mater Sci 2006;37:1507–18. https://doi.org/10.1007/s11661-006-0095-x.

[9] McDowell DL, Dunne FPE. Microstructure-sensitive computational modeling of fatigue crack formation. Int J Fatigue 2010;32:1521–42. https://doi.org/10.1016/j.ijfatigue.2010.01.003.

[10] Pilchak AL, Brandes MC, Williams REA, Williams JC. Investigation of faceted crack initiation and propagation in near-alpha titanium alloys. Ti-2011 2011:1–4.
[11] Ghosh S, Mills MJ, Rokhlin S, Sinha V, Soboyejo W, Williams JC. DOT/FAA/AR-06/24: The Evaluation of Cold Dwell Fatigue in Ti-6242. FAA Report 2007:1–375.
[12] Pilchak AL, Porter WJ, John R. Room temperature fracture processes of a near-alpha titanium alloy following elevated temperature exposure. J Mater Sci 2012;47:7235–53. https://doi.org/10.1007/s10853-012-6673-y.
[13] Ozturk D, Pilchak AL, Ghosh S. Experimentally validated dwell and cyclic fatigue crack nucleation model for α–titanium alloys. Scr Mater 2017;127:15–8. https://doi.org/10.1016/j.scriptamat.2016.08.031.
[14] Chen B, Jiang J, Dunne FPE. Is stored energy density the primary meso-scale mechanistic driver for fatigue crack nucleation? Int J Plast 2018;101:213–29. https://doi.org/10.1016/j.ijplas.2017.11.005.
[15] Wan VVC, Jiang J, MacLachlan DW, Dunne FPE. Microstructure-sensitive fatigue crack nucleation in a polycrystalline Ni superalloy. Int J Fatigue 2016;90:181–90. https://doi.org/10.1016/j.ijfatigue.2016.04.013.
[16] Fatemi A, Socie DF. A critical plane approach to multiaxial fatigue damage including out-of-phase loading. Fatigue Fract Eng Mater Struct 1988;11:149–65. https://doi.org/10.1111/j.1460-2695.1988.tb01169.x.
[17] Ozturk D, Kotha S, Pilchak AL, Ghosh S. Two-way multi-scaling for predicting fatigue crack nucleation in titanium alloys using parametrically homogenized constitutive models. J Mech Phys Solids 2019;128:181–207. https://doi.org/10.1016/j.jmps.2019.04.009.
[18] Chen B, Jiang J, Dunne FPE. Microstructurally-sensitive fatigue crack nucleation in Ni-based single and oligo crystals. J Mech Phys Solids 2017;106:15–33. https://doi.org/10.1016/j.jmps.2017.05.012.
[19] Ozturk D, Shahba A, Ghosh S. Crystal plasticity FE study of the effect of thermo-mechanical loading on fatigue crack nucleation in titanium alloys. Fatigue Fract Eng Mater Struct 2016:752–69. https://doi.org/10.1111/ffe.12410.
[20] Zheng Z, Stapleton A, Fox K, Dunne FPE. Understanding thermal alleviation in cold dwell fatigue in titanium alloys. Int J Plast 2018;111:234–52. https://doi.org/10.1016/j.ijplas.2018.07.018.
[21] Liu Y, Dunne FPE. The mechanistic link between macrozones and dwell fatigue in titanium alloys. Int J Fatigue 2021;142:105971. https://doi.org/10.1016/j.ijfatigue.2020.105971.
[22] Zhang Z, Dunne FPEE. Phase morphology, variants and crystallography of alloy microstructures in cold dwell fatigue. Int J Fatigue 2018;113:324–34. https://doi.org/10.1016/j.ijfatigue.2018.03.030.
[23] Venkataramani G, Kirane K, Ghosh S. Microstructural parameters affecting creep induced load shedding in Ti-6242 by a size dependent crystal plasticity FE model. Int J Plast 2008;24:428–54. https://doi.org/10.1016/j.ijplas.2007.05.001.
[24] Guo Y, Britton TB, Wilkinson AJ. Slip band-grain boundary interactions in commercial-purity titanium. Acta Mater 2014;76:1–12. https://doi.org/10.1016/j.actamat.2014.05.015.
[25] Sangid MD, Ezaz T, Sehitoglu H, Robertson IM. Energy of slip transmission and nucleation at grain boundaries. Acta Mater 2011;59:283–96. https://doi.org/10.1016/j.actamat.2010.09.032.
[26] Joseph S, Joseph K, Lindley TC, Dye D. The role of dwell hold on the dislocation mechanisms of fatigue in a near alpha titanium alloy. Int J Plast 2019;131. https://doi.org/10.1016/j.ijplas.2020.102743.

[27] Joseph S, Lindley TC, Dye D. Dislocation interactions and crack nucleation in a fatigued near-Alpha titanium alloy. Int J Plast 2018;110:38–56. https://doi.org/10.1016/j.ijplas.2018.06.009.
[28] Joseph S, Bantounas I, Lindley TC, Dye D. Slip transfer and deformation structures resulting from the low cycle fatigue of near-alpha titanium alloy Ti-6242Si. Int J Plast 2018;100:90–103. https://doi.org/10.1016/j.ijplas.2017.09.012.
[29] Lee TC, Robertson IM, Birnbaum HK. An In Situ transmission electron microscope deformation study of the slip transfer mechanisms in metals. Metallurgical Transactions A 1990;21:2437–47. https://doi.org/10.1007/BF02646988.
[30] Liu Y, Zhang X, Zhu Y, Hu P, Oskay C. Dislocation density informed eigenstrain based reduced order homogenization modeling: Verification and application on a titanium alloy structure subjected to cyclic loading. Model Simul Mat Sci Eng 2020;28. https://doi.org/10.1088/1361-651X/ab602e.
[31] Zhang X, Oskay C. Eigenstrain based reduced order homogenization for polycrystalline materials. Comput Methods Appl Mech Eng 2015;297:408–36. https://doi.org/10.1016/j.cma.2015.09.006.
[32] Zhang X, Liu Y, Oskay C. Multiscale Reduced-Order Modeling of a Titanium Skin Panel Subjected to Thermo-Mechanical Loading. AIAA 2020:1–25.
[33] Zhang X, Oskay C. Sparse and scalable eigenstrain-based reduced order homogenization models for polycrystal plasticity. Comput Methods Appl Mech Eng 2017;326:241–69. https://doi.org/10.1016/j.cma.2017.07.027.
[34] Zhang X, Liu Y, Oskay C. Uncertainty Quantification for Microstructure-Sensitive Fatigue Nucleation and Application to Titanium Alloy, Ti6242. Front Mater 2022;9:1–17. https://doi.org/10.3389/fmats.2022.897998.
[35] Zhang Z, Dunne FPEE. Microstructural heterogeneity in rate-dependent plasticity of multiphase titanium alloys. J Mech Phys Solids 2017;103:199–220. https://doi.org/10.1016/j.jmps.2017.03.012.
[36] Arsenlis A, Parks DM. Crystallographic aspects of geometrically-necessary and statistically-stored dislocation density. Acta Mater 1999;47:1597–611. https://doi.org/10.1016/S1359-6454(99)00020-8.
[37] Nye JF. Some geometrical relations in dislocated crystals. Acta Metallurgica 1953;1:153–62. https://doi.org/10.1016/0001-6160(53)90054-6.
[38] Xu Y, Joseph S, Karamched P, Fox K, Rugg D, Dunne FPE, et al. Predicting dwell fatigue life in titanium alloys using modelling and experiment. Nat Commun 2020;11:5868. https://doi.org/10.1038/s41467-020-19470-w.
[39] Beyerlein IJ, Tomé CN. A dislocation-based constitutive law for pure Zr including temperature effects. Int J Plast 2008;24:867–95. https://doi.org/10.1016/j.ijplas.2007.07.017.
[40] Cheng J, Shahba A, Ghosh S. Stabilized tetrahedral elements for crystal plasticity finite element analysis overcoming volumetric locking. Comput Mech 2016;57:733–53. https://doi.org/10.1007/s00466-016-1258-2.
[41] Ma A, Roters F, Raabe D. A dislocation density based constitutive model for crystal plasticity FEM including geometrically necessary dislocations. Acta Mater 2006;54:2169–79. https://doi.org/10.1016/j.actamat.2006.01.005.
[42] Madec R, Devincre B, Kubin LP. From Dislocation Junctions to Forest Hardening. Phys Rev Lett 2002;89:1–4. https://doi.org/10.1103/PhysRevLett.89.255508.
[43] Gockel BT, Kolesar RS, Rollett AD. Experimental study of an aerospace titanium alloy under various thermal and tensile loading rate conditions. Integr Mater Manuf Innov 2016;5:245–58. https://doi.org/10.1186/s40192-016-0057-0.

[44] Evers LP, Brekelmans WAM, Geers MGD. Non-local crystal plasticity model with intrinsic SSD and GND effects. J Mech Phys Solids 2004;52:2379–401. https://doi.org/10.1016/j.jmps.2004.03.007.
[45] Evers LP, Brekelmans WAM, Geers MGD. Scale dependent crystal plasticity framework with dislocation density and grain boundary effects. Int J Solids Struct 2004;41:5209–30. https://doi.org/10.1016/j.ijsolstr.2004.04.021.
[46] Evers LP, Parks DM, Brekelmans WAM, Geers MGD. Crystal plasticity model with enhanced hardening by geometrically necessary dislocation accumulation. J Mech Phys Solids 2002;50:2403–24. https://doi.org/10.1016/S0022-5096(02)00032-7.
[47] Forest S. Some links between Cosserat, strain gradient crystal plasticity and the statistical theory of dislocations. Philosophical Magazine 2008;88:3549–63. https://doi.org/10.1080/14786430802154815.
[48] Zirkle T, Zhu T, McDowell DL. Micromechanical crystal plasticity back stress evolution within FCC dislocation substructure. Int J Plast 2021;146. https://doi.org/10.1016/j.ijplas.2021.103082.
[49] Liu Y, Zhang X, Zhu Y, Hu P, Oskay C. Dislocation density informed eigenstrain based reduced order homogenization modeling: Verification and application on a titanium alloy structure subjected to cyclic loading. Model Simul Mat Sci Eng 2020;28. https://doi.org/10.1088/1361-651X/ab602e.
[50] Kitayama K, Tomé CN, Rauch EF, Gracio JJ, Barlat F. A crystallographic dislocation model for describing hardening of polycrystals during strain path changes. Application to low carbon steels. Int J Plast 2013;46:54–69. https://doi.org/10.1016/j.ijplas.2012.09.004.
[51] Gockel BT, Kolesar RS, Rollett AD. Experimental study of an aerospace titanium alloy under various thermal and tensile loading rate conditions. Integr Mater Manuf Innov 2016;5:245–58. https://doi.org/10.1186/s40192-016-0057-0.
[52] Zhang T, Collins DM, Dunne FPE, Shollock BA. Crystal plasticity and high-resolution electron backscatter diffraction analysis of full-field polycrystal Ni superalloy strains and rotations under thermal loading. Acta Mater 2014;80:25–38. https://doi.org/10.1016/j.actamat.2014.07.036.
[53] Zhang Z, Jun TS, Britton TB, Dunne FPE. Determination of Ti-6242 α and β slip properties using micro-pillar test and computational crystal plasticity. J Mech Phys Solids 2016;95:393–410. https://doi.org/10.1016/j.jmps.2016.06.007.
[54] Bachmann F, Hielscher R, Schaeben H. Grain detection from 2d and 3d EBSD data-Specification of the MTEX algorithm. Ultramicroscopy 2011;111:1720–33. https://doi.org/10.1016/j.ultramic.2011.08.002.
[55] Eghtesad A, Barrett TJ, Knezevic M. Compact reconstruction of orientation distributions using generalized spherical harmonics to advance large-scale crystal plasticity modeling: Verification using cubic, hexagonal, and orthorhombic polycrystals. Acta Mater 2018;155:418–32. https://doi.org/10.1016/j.actamat.2018.06.017.
[56] Quey R, Dawson PR, Barbe F. Large-scale 3D random polycrystals for the finite element method: Generation, meshing and remeshing. Comput Methods Appl Mech Eng 2011;200:1729–45. https://doi.org/10.1016/j.cma.2011.01.002.
[57] Kotha S, Ozturk D, Ghosh S. Parametrically homogenized constitutive models (PHCMs) from micromechanical crystal plasticity FE simulations, part I: Sensitivity analysis and parameter identification for Titanium alloys. Int J Plast 2019;120:296–319. https://doi.org/10.1016/j.ijplas.2019.05.008.

[58] Kotha S, Ozturk D, Ghosh S. Uncertainty-quantified parametrically homogenized constitutive models (UQ-PHCMs) for dual-phase α/β titanium alloys. NPJ Comput Mater 2020;6. https://doi.org/10.1038/s41524-020-00379-3.
[59] Williams JC, Baggerly RG, Paton NE. Deformation behavior of HCP Ti-Al alloy single crystals. Metallurgical and Materials Transactions A 2002;33:837–50. https://doi.org/10.1007/s11661-002-0153-y.
[60] Castelluccio GM, McDowell DL. Effect of annealing twins on crack initiation under high cycle fatigue conditions. J Mater Sci 2013;48:2376–87. https://doi.org/10.1007/s10853-012-7021-y.
[61] Smith BD, Shih DS, McDowell DL. Fatigue hot spot simulation for two Widmanstätten titanium microstructures. Int J Fatigue 2016;92:116–29. https://doi.org/10.1016/j.ijfatigue.2016.05.002.
[62] Dunne FPE, Wilkinson AJ, Allen R. Experimental and computational studies of low cycle fatigue crack nucleation in a polycrystal. Int J Plast 2007;23:273–95. https://doi.org/10.1016/j.ijplas.2006.07.001.
[63] Cheong KS, Busso EP. Effects of lattice misorientations on strain heterogeneities in FCC polycrystals. J Mech Phys Solids 2006;54:671–89. https://doi.org/10.1016/j.jmps.2005.11.003.
[64] Wilkinson AJ. Examination of fatigue crack plastic zones using scanning-electron-microscope-based electron diffraction techniques. Philos Mag Lett 1996;74:145–52. https://doi.org/10.1080/095008396180290.
[65] Ahmed J, Wilkinson AJ, Roberts SG. Electron channelling contrast imaging characterization of dislocation structures associated with extrusion and intrusion systems and fatigue cracks in copper single crystals. Philosophical Magazine A 2001;81:1473–88. https://doi.org/10.1080/01418610108214358.
[66] Kirane K, Ghosh S. A cold dwell fatigue crack nucleation criterion for polycrystalline Ti-6242 using grain-level crystal plasticity FE Model. Int J Fatigue 2008;30:2127–39. https://doi.org/10.1016/j.ijfatigue.2008.05.026.
[67] Wan VVC, Maclachlan DW, Dunne FPE. A stored energy criterion for fatigue crack nucleation in polycrystals. Int J Fatigue 2014;68:90–102. https://doi.org/10.1016/j.ijfatigue.2014.06.001.
[68] Wang Z, Garbe U, Li H, Harrison RP, Kaestner A, Lehmann E. Observations on the zirconium hydride precipitation and distribution in Zircaloy-4. Metallurgical and Materials Transactions B: Process Metallurgy and Materials Processing Science 2014;45:532–9. https://doi.org/10.1007/s11663-013-9866-0.
[69] Wan VVC, Cuddihy MA, Jiang J, Maclachlan DW, Dunne FPE. An HR-EBSD and computational crystal plasticity investigation of microstructural stress distributions and fatigue hotspots in polycrystalline copper. Acta Mater 2016;115:45–57. https://doi.org/10.1016/j.actamat.2016.05.033.
[70] Wan VVCC, MacLachlan DW, Dunne FPEE. Integrated experiment and modelling of microstructurally-sensitive crack growth. Int J Fatigue 2016;91:110–23. https://doi.org/10.1016/j.ijfatigue.2016.05.027.
[71] Xu Y, Wan W, Dunne FPE. Microstructural fracture mechanics: stored energy density at fatigue cracks. J Mech Phys Solids 2020:104209. https://doi.org/10.1016/j.jmps.2020.104209.
[72] Kim J-Y, Rokhlin SI. Determination of elastic constants of generally anisotropic inclined lamellar structure using line-focus acoustic microscopy. J Acoust Soc Am 2009;126:2998–3007. https://doi.org/10.1121/1.3245032.

[73] Zhang Z, Jun TS, Britton TB, Dunne FPE. Intrinsic anisotropy of strain rate sensitivity in single crystal alpha titanium. Acta Mater 2016;118:317–30. https://doi.org/10.1016/j.actamat.2016.07.044.
[74] Lavenstein S, Gu Y, Madisetti D, El-Awady JA. The heterogeneity of persistent slip band nucleation and evolution in metals at the micron scale. Science (1979) 2020;190. https://doi.org/10.1126/science.abb2690.
[75] Wilkinson AJ, Henderson MB, Martin JW. Examination of fatigue crack plastic zones using scanning-electron-microscope-based electron diffraction techniques. Philos Mag Lett 1996;74:145–52. https://doi.org/10.1080/095008396180290.
[76] Ahmed J, Wilkinson AJ, Roberts SG. Electron channelling contrast imaging characterization of dislocation structures associated with extrusion and intrusion systems and fatigue cracks in copper single crystals. Philosophical Magazine A: Physics of Condensed Matter, Structure, Defects and Mechanical Properties 2001;81:1473–88. https://doi.org/10.1080/01418610108214358.
[77] Ghosh S, Chakraborty P. Microstructure and load sensitive fatigue crack nucleation in Ti-6242 using accelerated crystal plasticity FEM simulations. Int J Fatigue 2013;48:231–46. https://doi.org/10.1016/j.ijfatigue.2012.10.022.
[78] Parvatareddy H, Dillard DA. Effect of mode-mixity on the fracture toughness of Ti-6Al-4V/FM-5 adhesive joints. Int J Fract 1999;96:215–28. https://doi.org/10.1023/A:1018609418627.
[79] Camilo CC, de Souza EC, di Lorenzo PL, Rollo JMD de A. Measurement of the grain boundary energy of commercially-pure grade 2 titanium at high temperature. Revista Brasileira de Engenharia Biomedica 2011;27:175–81. https://doi.org/10.4322/rbeb.2011.014.
[80] Przybyla CP, McDowell DL. Simulated microstructure-sensitive extreme value probabilities for high cycle fatigue of duplex Ti-6Al-4V. Int J Plast 2011;27:1871–95. https://doi.org/10.1016/j.ijplas.2011.01.006.
[81] Briffod F, Shiraiwa T, Enoki M. A Nucleation and propagation modeling of short fatigue crack in rolled bi-modal Ti – 6Al – 4V alloy. Materials Science & Engineering A 2020;790:139710. https://doi.org/10.1016/j.msea.2020.139710.
[82] McDowell DL. Simulation-based strategies for microstructure-sensitive fatigue modeling. Materials Science and Engineering A 2007;468–470:4–14. https://doi.org/10.1016/j.msea.2006.08.129.
[83] Zheng Z, Balint DS, Dunne FPE. Discrete dislocation and crystal plasticity analyses of load shedding in polycrystalline titanium alloys. Int J Plast 2016;87:15–31. https://doi.org/10.1016/j.ijplas.2016.08.009.
[84] Xu Y, Fox K, Rugg D, Dunne FPE. Cyclic plasticity and thermomechanical alleviation in titanium alloys. Int J Plast 2020;134:102753. https://doi.org/10.1016/j.ijplas.2020.102753.
[85] Liu Y, Adande S, Britton TB, Dunne FPE. Cold dwell fatigue analyses integrating crystal-level strain rate sensitivity and microstructural heterogeneity. Int J Fatigue 2021;151:106398. https://doi.org/10.1016/j.ijfatigue.2021.106398.
[86] Lin M, Liu Y, Oskay C, Zhang X. Toward Microstructure-Informed Reduced-Order Modeling of Fatigue Initiation in a Titanium Skin Panel Subjected to Thermo-Mechanical Loading. AIAA Science and Technology Forum and Exposition, AIAA SciTech Forum 2022 2022. https://doi.org/10.2514/6.2022-0210.
[87] Zheng Z, Zhao P, Zhan M, Shen S, Wang Y, Fu MW. The roles of rise and fall time in load shedding and strain partitioning under the dwell fatigue of titanium alloys with different microstructures. Int J Plast 2022;149. https://doi.org/10.1016/j.ijplas.2021.103161.

[88] Morrissey RJ, Mcdowell DL, Nicholas T. Frequency and stress ratio effects in high cycle fatigue of Ti-6Al-4V. vol. 21. 1999.
[89] Stopka KS, McDowell DL. Microstructure-Sensitive Computational Estimates of Driving Forces for Surface Versus Subsurface Fatigue Crack Formation in Duplex Ti-6Al-4V and Al 7075-T6. Jom 2020;72:28–38. https://doi.org/10.1007/s11837-019-03804-1.
[90] Gu T, Stopka KS, Xu C, McDowell DL. Prediction of maximum fatigue indicator parameters for duplex Ti–6Al–4V using extreme value theory. Acta Mater 2020;188:504–16. https://doi.org/10.1016/j.actamat.2020.02.009.
[91] Zheng Z, Balint DS, Dunne FPE. Rate sensitivity in discrete dislocation plasticity in hexagonal close-packed crystals. Acta Mater 2016;107:17–26. https://doi.org/10.1016/j.actamat.2016.01.035.
[92] Dunne FPE, Walker A, Rugg D. A systematic study of hcp crystal orientation and morphology effects in polycrystal deformation and fatigue. Proceedings of the Royal Society A: Mathematical, Physical and Engineering Sciences 2007;463:1467–89. https://doi.org/10.1098/rspa.2007.1833.
[93] Sinha V, Schwarz RB, Mills MJ, Williams JC. Influence of hydrogen on dwell-fatigue response of near-alpha titanium alloys. Acta Mater 2020;188:315–27. https://doi.org/10.1016/j.actamat.2019.12.025.
[94] Cuddihy MA, Stapleton A, Williams S, Dunne FPE. On cold dwell facet fatigue in titanium alloy aero-engine components. Int J Fatigue 2017;97:177–89. https://doi.org/10.1016/j.ijfatigue.2016.11.034.
[95] Sinha V, Mills MJ, Williams JC. Crystallography of fracture facets in a near-alpha titanium alloy. Metallurgical and Materials Transactions A 2006;37:2015–26. https://doi.org/10.1007/s11661-006-0144-5.
[96] Harr ME, Daly S, Pilchak AL. The effect of temperature on slip in microtextured Ti-6Al-2Sn-4Zr-2Mo under dwell fatigue. Int J Fatigue 2021;147:106173. https://doi.org/10.1016/j.ijfatigue.2021.106173.
[97] Sinha V, Pilchak AL, Jha SK, Porter WJ, John R, Larsen JM. Correlating Scatter in Fatigue Life with Fracture Mechanisms in Forged Ti-6242Si Alloy. Metall Mater Trans A Phys Metall Mater Sci 2018;49:1061–78. https://doi.org/10.1007/s11661-017-4437-7.
[98] Pilchak AL, Williams JC. Observations of Facet Formation in Near-α Titanium and Comments on the Role of Hydrogen. Metallurgical and Materials Transactions A 2011;42:1000–27. https://doi.org/10.1007/s11661-010-0507-9.
[99] Davidson DL, Eylon D. Titanium alloy fatigue fracture facet investigation by selected area electron channeling. Metallurgical Transactions A 1980;11:837–43. https://doi.org/10.1007/BF02661213.
[100] Uta E, Gey N, Bocher P, Humbert M, Gilgert J. Texture heterogeneities in αp/αs titanium forging analysed by EBSD-Relation to fatigue crack propagation. J Microsc 2009;233:451–9. https://doi.org/10.1111/j.1365-2818.2009.03141.x.
[101] Tanaka K, Mura T. A dislocation model for fatigue crack initiation. J Appl Mech 1981;48:97–103. https://doi.org/10.1115/1.3157599.
[102] Kitayama K, Tomé CN, Rauch EF, Gracio JJ, Barlat F. A crystallographic dislocation model for describing hardening of polycrystals during strain path changes. Application to low carbon steels. Int J Plast 2013;46:54–69. https://doi.org/10.1016/j.ijplas.2012.09.004.
[103] Zecevic M, Knezevic M. A dislocation density based elasto-plastic self-consistent model for the prediction of cyclic deformation: Application to AA6022-T4. Int J Plast 2015;72:200–17. https://doi.org/10.1016/j.ijplas.2015.05.018.

[104] Knezevic M, McCabe RJ, Lebensohn RA, Tomé CN, Liu C, Lovato ML, et al. Integration of self-consistent polycrystal plasticity with dislocation density based hardening laws within an implicit finite element framework: Application to low-symmetry metals. J Mech Phys Solids 2013;61:2034–46. https://doi.org/10.1016/j.jmps.2013.05.005.
[105] Viguier B, Cieslar M, Bonneville J, Hemker KJ, Martin JL, Tms. Deformation mechanisms in polycrystalline gamma TiAl. Proceedings of the 1995 124th TMS Annual Meeting, 1995.
[106] Naka M, Okamoto I, Arata Y. Joining mechanism of ceramics to metals using an amorphous titaniu-based filler metal. Materials Science and Engineering 1988. https://doi.org/10.1016/0025-5416(88)90195-4.
[107] Williams WS, Schaal RD. Elastic deformation, plastic flow, and dislocations in single crystals of titanium carbide. J Appl Phys 1962;33:955–62. https://doi.org/10.1063/1.1777197.
[108] Appel F, Paul JDH, Oehring M, Fröbel U, Lorenz U. Creep behavior of TiAl alloys with enhanced high-temperature capability. Metall Mater Trans A Phys Metall Mater Sci 2003;34 A:2149–64. https://doi.org/10.1007/s11661-003-0279-6.
[109] Liu Y, Wan W, Dunne FPE. Characterisation and modelling of micro- and macroscale creep and strain rate sensitivity in Zircaloy-4. Materials Science and Engineering: A 2022:142981. https://doi.org/10.1016/j.msea.2022.142981.

Appendix A Reversal dislocation evolution in CP

During cyclic load, the dislocation evolution in the microstructure is schematically illustrated in Fig A1. While applying the load along the coupon test specimen, the grain lattice is distorted by the incompatible plastic deformation inside individual grain with different crystallographic orientations shown in Fig A1 (a). The geometrically-necessary dislocation (GND) accumulates near the grain boundaries to accommodate the lattice distortion due to grain interactions, which is computed by the curl of the plastic deformation gradient in Eq. (6).

During the load-up, dislocations are activated in certain slip systems and pinned by the local microstructural defects inside the grain and the sessile dislocations are divided into forest dislocation and dislocation debris shown in Fig A1 (b). The forest dislocation is partially reversible due to the higher lattice friction stress against dislocation motion in the reverse direction than in the forward direction [101], which has been experimentally observed and discussed in the framework of TEM studies [27]. Here, we assume that the complete reversal is not possible and the irreversible forest dislocation remains inside the grain shown in Fig A1 (b). Following Eq. (6), the evolution of the forward forest dislocation is expressed as,

$$\frac{\partial \rho_{\mathrm{fwd}}^{\kappa}}{\partial \gamma^{\kappa}} = (1-p)k_1^{\kappa}\sqrt{\rho_{\mathrm{for}}^{\kappa}} - k_2^{\kappa}\rho_{\mathrm{for}}^{\kappa} \tag{A.1}$$

where the value p is a reversibility parameter, which determines the fraction of the reversible loosely tangled forest dislocations. Here, the p = 0.8 is chosen to obtain the relatively low dislocation debris density [102] for near-α titanium alloys from the TEM observations [27]. k_1^κ and k_2^κ are the dislocation generating coefficient and the annihilation coefficient due to dynamic recovery, respectively and their relationship have been reported in [30]. The evolution of reversible forest dislocations are expressed as a function of the local resolved shear stress,

$$\begin{aligned}\frac{\partial \rho_{\text{rev}}^{\kappa+}}{\partial \gamma^\kappa} &= \left\{\frac{\tau^\kappa}{|\tau^\kappa|}\right\}\left(pk_1^\kappa\sqrt{\rho_{\text{for}}^\kappa} - k_2^\kappa \rho_{\text{rev}}^{\kappa+}\right) - \left\{-\frac{\tau^\kappa}{|\tau^\kappa|}\right\} k_1^\kappa \sqrt{\rho_{\text{for}}^\kappa}\left(\frac{\rho_{\text{rev}}^{\kappa+}}{\rho_0^\kappa}\right)^{\hat{m}} \\ \frac{\partial \rho_{\text{rev}}^{\kappa-}}{\partial \gamma^\kappa} &= \left\{-\frac{\tau^\kappa}{|\tau^\kappa|}\right\}\left(pk_1^\kappa\sqrt{\rho_{\text{for}}^\kappa} - k_2^\kappa \rho_{\text{rev}}^{\kappa-}\right) - \left\{\frac{\tau^\kappa}{|\tau^\kappa|}\right\} k_1^\kappa \sqrt{\rho_{\text{for}}^\kappa}\left(\frac{\rho_{\text{rev}}^{\kappa-}}{\rho_0^\kappa}\right)^{\hat{m}}\end{aligned} \tag{A.2}$$

where symbol {} is the Macaulay brackets. ρ_0^κ is the value of the total dislocation density at the point of load reversal and $\hat{m}$ is the dislocation density recombination coefficient taken to be 0.4 for HCP and BCC crystals [103].

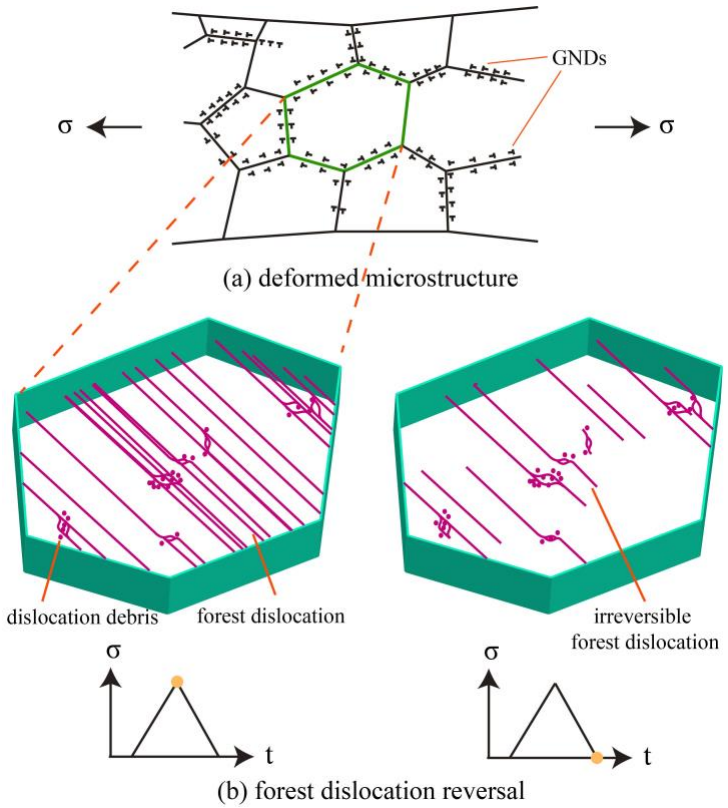

Fig A1 shows the schematic illustration of dislocation evolution in the microstructure, including (a) the GND accumulation near the grain boundaries in the deformed grain structures and (b) the reversible forest dislocation during the load reversal.

The dislocation debris is the dislocation loop generated from dislocation interactions and embedded in the grain substructure, which is at the near atomic dimension and irreversible shown in Fig A1 (b). The evolution of dislocation debris is defined as,

$$\frac{\partial \rho_{\mathrm{deb}}}{\partial \gamma^{\kappa}} = \sum_{\kappa} q b^{\kappa} \sqrt{\rho_{\mathrm{deb}}}\, k_2^{\kappa}\, \rho_{\mathrm{for}}^{\kappa} \tag{A.1}$$

where q is the rate coefficient defining the fraction of dislocations that do not annihilate but stored as debris [104].

The initial forest dislocation is relatively low after the annealing process [51] and set as 1.0×10^{12} mm^{-2} consistent with experimental observations [53,105,106]. Debris dislocation mainly generates from forest dislocation interaction, which leads to its relatively lower density, set as 1.0×10^{10} mm^{-2} [107,108]. It is known that the dislocation pile up near inclusion grains and phase boundaries where dislocation densities are high. In this study, the microstructure reconstruction is based on Ti-6242S [51], of which inclusion percentage is quite low. The β phase usually works as a slip transferring medium between the alpha grains [53] and β phase only occupies less than 6% in the microstructure without colony structure. It is anticipated that β phase barely contributes to the major dislocation density increase near grain boundaries between primary α, which is the main reason for homogenized α RVE reconstruction.

Appendix B Mesh sensitivity study

Mesh sensitivity is conducted for the different SVEs generated from NEPER [56]. Relative element lengths (RCLs) is used to change the mesh size, i.e. the relative characteristic length, whose value is relative to the average cell size of Voronoi tessellation [56]. Tetrahedral (tet) and hexahedral (hex) meshes are investigated at different RCLs = 0.5, 0.65, 0.8 and 1. Quadratic mesh types are chosen for tet (C3D10) and hex (C3D20). Fig A2 (a-h) shows the increase of the mesh density when RCL drops for both tet and hex meshes.

Fig A2 (g) shows that the mesh convergence could always be reached in quadratic hex mesh whereas slight increase of stress value is observed when RCL = 0.8 and 1 for quadratic tet mesh. The finding is consistent with former mesh studies of another type of HCP crystal alloy, i.e. zirconium alloy [109]. C3D10 elements would relieve the volumetric locking effect, but the locking still exists when its mesh density is too low, which leads to limited degrees of freedom for capturing the geometric nonlinearity.

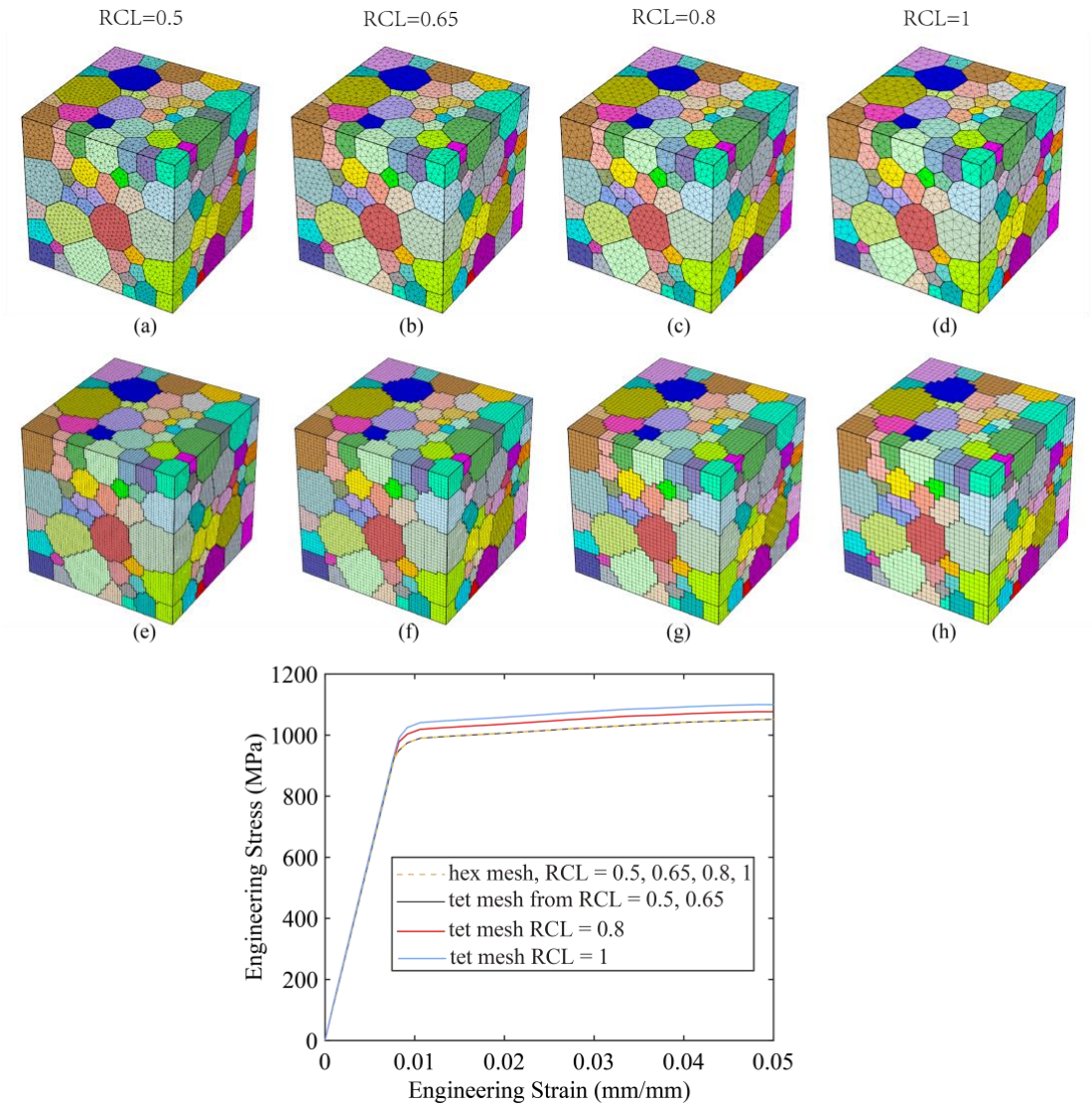

Fig A2. Mesh size studies at different RCLs for tetrahedral and hexahedral element types.

To validate the mesh sensitivity of FIPs, the value and location of the highest FIP magnitude R_η (η=ε, MD3, Mix, SED and FS) are extracted in the worst-case hard-soft grain pair set-up in Fig 4 under dwell fatigue case, regarding hex mesh sizes RCLs = 0.5, 0.65, 0.8 and 1 in Fig. A2 (e-h). The case of RCL = 0.8 with element size of 0.5 μm is defined as the reference case. Distances ΔD_{RCL} and the percentage differences $\Delta R_{\eta,\,RCL}$ (%) are extracted in Table A1, between the reference case and the other cases with different mesh sizes.

It is noticed that largest differences occur in the location and value between reference case and RCL=1.0, compared with reference case of RCL = 0.8. The distances ΔD_{RCL} are up to ~2-5 μm for all the FIPs, close or even higher than the average grain size ~3 μm, and the uncertainty lies in the location of maximum R_η when comparing cases between RCL = 0.8 and 1. The maximum value has a difference $\Delta R_{\eta,\,RCL}$ of ~20-35% for all the FIPs showing a significant difference

between RCL = 0.8 and 1. R_{Mix} has the largest location difference and R_{FS} has the highest value difference.

These differences drop significantly when the RCL = 0.65 where all the distances ΔD_{RCL} are less than 1 μm and the maximum value changes $\Delta R_{\eta, RCL}$ are less than 10%. This trend remains the same for RCL = 0.5. This means the location and value stabilise when RCL is in the range of [0.5, 0.8]. Overall, aiming to efficiently capture accurate local responses of FIPs, i.e. R_η (η=ε, MD3, Mix, SED and FS), the mesh sensitivity study leads to the choice of quadratic hexahedral element (C3D20R) and element size of 0.5 μm, i.e. RCL=0.8 (6 times lower than average grain size).

Table A1. Mesh size studies at different RCLs for hex element under dwell fatigue case

	RCL=1.0	RCL=0.65	RCL=0.5	ΔD_{RCL} (μm) / $\Delta R_{\eta, RCL}$ (%) Reference case: RCL=0.8
R_ε	2.0 / 21	0.4 / 5	0.4 / 4	
R_{MD3}	2.4 / 21	0.5 / 3	0.6 / 2	
R_{Mix}	5.2 / 19	0.7 / 7	0.7 / 8	
R_{SED}	3.1 / 27	0.4 / 6	0.6 / 8	
R_{FS}	3.2 / 36	1.2 / 9	1.1/ 7	

Appendix C Relative length ratio study

A convergence study is conducted to validate the choice of the relative length ratio, such that the boundary effect of the cell on the grain pair response is negligible. In Fig A3, a simulation cell is constructed with a hard-soft grain pair inside a homogenized media. The homogenized exterior region is introduced to eliminate boundary effects from the analysis. The stress-strain response in the homogenized region (outside the grain pair) of near-α Ti-6242S, is idealized using a bi-linear isotropic elasto-plastic model yielding 1030 MPa and the flow stress reaches 1120 MPa at 9% effective plastic strain, matching the ambient temperature uniaxial tensile data of Ti-6242S [51]. Transverse elasticity is applied to describe the anisotropic elastic behavior of the homogenized region shown in Table 1.

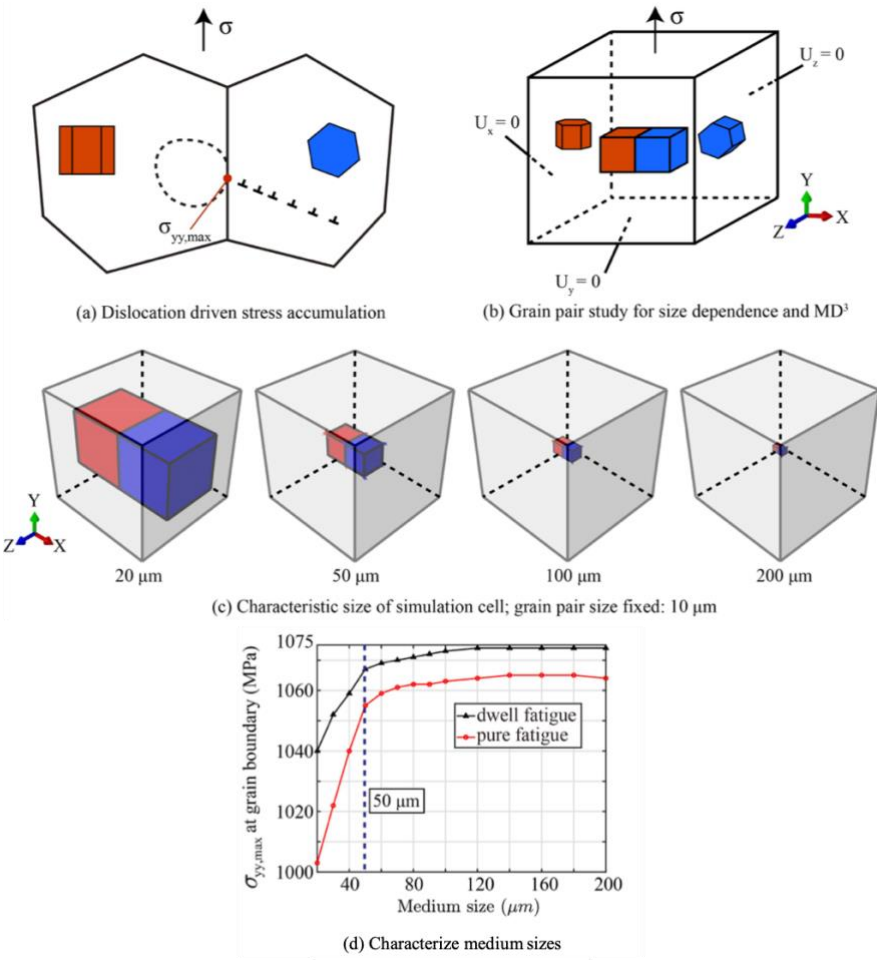

Fig A3 Relative length ratio study. (a) the grain-pair model proposed by Stroh [4]*; (b) the grain-pair study in CPFE framework for size dependence; (c) the characteristic sizes of cells with grain-pair size fixed at 10 μm; (d) the maximum basal stress in hard grain versus characteristic sizes at 10th cycle.*

The grain size is fixed at 10 μm. The characteristic sizes of simulation cell range from 20 μm to 200 μm with increments of 10 μm, and the exemplary grain pairs and simulation cells are shown in Fig A3 (c) with relative length ratio ranging from 0.5 to 0.05. Dwell fatigue and pure fatigue loading conditions are the same as Fig 4 (a, b). The stress hold time is set to 2 min in dwell fatigue. The accumulated maximum basal stress $\sigma_{yy,max}$ in the hard grain (near hard-soft grain boundary) is studied over all the simulation cells for the two loading conditions. The stress $\sigma_{yy,max}$ versus the characteristic size is shown in Fig A3 (d), at the 10th cycle of the dwell and pure fatigue loads. Stress $\sigma_{yy,max}$ stabilizes when the characteristic size is larger than 50 μm and tends to decrease when size decreases from 50 to 20 μm. This demonstrates that a cell size of >~ 50 μm, i.e. relative length ratio <~0.2 is suitable for eliminating the boundary effect while maintaining relatively low computational cost.